

Symmetry-broken superconducting configurations from density functional theory for bcc and hcp metals and Nb₃Sn

Shun-Li Shang and Zi-Kui Liu

Department of Materials Science and Engineering, The Pennsylvania State University,
University Park, PA 16802, USA

Abstract:

We recently proposed a unified theoretical framework for superconductivity that broadens the applicability of Bardeen-Cooper-Schrieffer (BCS) theory to both conventional and unconventional superconductors. Within this framework, superconductivity arises from the formation of a *symmetry-broken* superconducting configuration (SCC) generated by atomic perturbations of the normal conducting configuration (NCC). The SCC emerges through electron-phonon interaction and gives rise to distinct straight one-dimensional tunnels (SODTs) in the charge density difference of electrons and/or holes. These SODTs originate from regular and systematic atomic displacements between the SCC and NCC, a phenomenon revealed by density functional theory (DFT) calculations. To further verify this framework, we performed DFT-based calculations for 12 hexagonal close-packed (hcp) elements (Be, Mg, Sc, Y, Ti, Zr, Hf, Tc, Re, Ru, Os, and Zn), 5 body-centered cubic (bcc) elements (V, Nb, Ta, Mo, and W), and the compound Nb₃Sn. Our results indicate that all these materials exhibit superconductivity at 0 K and 0 GPa, as evidenced by the predicted SODTs. Notably, Mg, Sc, and Y are predicted to be superconducting under ambient pressure, a finding that awaits experimental confirmation.

Keywords:

Bardeen-Cooper-Schrieffer (BCS) theory; Density functional theory (DFT); Superconducting configuration (SCC); Normal conducting configuration (NCC); Straight one-dimensional tunnels (SODTs); Pure element superconductors; Nb₃Sn

1 Introduction

Superconductivity was first discovered in 1911 by Heike Kamerlingh Onnes in mercury (Hg) at approximately 4.2 K [1]. Nearly half a century later, in 1957, Bardeen, Cooper, and Schrieffer (BCS) [2] developed the microscopic BCS theory to explain superconductivity as a quantum mechanical phenomenon in which electrons form pairs, known as Cooper pairs, below the material's critical temperature T_C . These pairs arise through electron-phonon interactions, mediated by lattice vibrations (phonons), enabling electrons to move without electrical resistance. However, superconductivity is inherently fragile due to the weak pairing interaction (on the order of a few meV); consequently, thermal energy can easily break Cooper pairs, limiting conventional superconductors to low T_C .

Building on BCS theory, McMillan proposed an approximate formula for the superconducting transition temperature (T_C) [3,4],

$$T_C = 0.85\Theta_D e^{-1/n(\epsilon_F)\phi_{el-ph}}, \quad Eq. 1$$

where Θ_D is the Debye temperature related to the highest vibrational frequency, $n(\epsilon_F)$ is the electronic density of states (eDOS) at the Fermi level, and ϕ_{el-ph} is the effective electron-phonon interaction [5,6]. According to Eq. 1, a superconductor must be a conductor with a nonzero $n(\epsilon_F)$. McMillan further concluded that T_C for conventional superconductors cannot exceed ~ 40 K under ambient pressure, since excessively increasing ϕ_{el-ph} destabilizes the lattice [3,7]. Recently, Liu and Shang [8] showed that BCS theory applies to both conventional and unconventional superconductors, noting that electron-phonon coupling may be localized near superconducting layers or directions. Their analysis of the layered “*pontoon*” structure in the high T_C superconductor $\text{YBa}_2\text{Cu}_3\text{O}_7$ (YBCO₇) suggests that weak bonding of superconducting layers to the bulk matrix provides thermal insulation, protecting Cooper pairs from disruption to higher temperatures.

The superconducting gap, representing the energy gain when two electrons form a Cooper pair, is related to T_C for conventional superconductors at 0 K and vanishes at T_C [9,10],

$$\Delta(T = 0K) = 1.764k_B T_C. \quad Eq. 2$$

This gap is directly linked to the energy difference between the superconducting configuration (SCC) and the normal conducting configuration (NCC), commonly called the condensation energy [2,11,12],

$$\Delta E_{SN} = -\frac{1}{2}n(\varepsilon_F)\Delta^2. \quad Eq. \ 3$$

Here, $\Delta E_{SN} < 0$ indicates that SCC is the ground state, while $\Delta E_{SN} > 0$ corresponds to a non-superconducting system.

A major theoretical advance after BCS theory was density functional theory (DFT), introduced by Hohenberg and Kohn [13] and Kohn and Sham [14]. DFT provides a practical solution to the many-body Schrödinger equation, enabling prediction of electron-phonon interaction (ϕ_{el-ph}) in Eq. 1 [15]. DFT asserts that any system has a unique ground-state electron density that minimizing its energy at 0 K [13]. Central to DFT is the exchange-correlation (X-C) functional, which is approximated using schemes such as the local density approximation (LDA), the generalized gradient approximation (GGA), and the meta-GGA [16].

Notably, Sun, Ruzsinszky, and Perdew [17] developed the first nonempirical meta-GGA of the Strongly Constrained and Appropriately Normed (SCAN) functional, satisfying all 17 known exact constraints. In SCAN, strong correlations within a symmetry-unbroken ground-state wavefunction can manifest as symmetry-broken spin or charge densities due to soft fluctuation modes. This concept of independent symmetry-broken configurations was interestingly envisioned by Gibbs in 1902 in developing statistical mechanics [18,19], who “imagined a great number of systems of the same nature, but differing in the configurations and velocities which they have at a given instant, and differing not merely infinitesimally, but it may be so as to embrace every conceivable combination of configuration and velocities”.

The main challenge in applying DFT to superconductors lies in identifying the SCC. Inspired by the ground-state electron density principle and the symmetry-breaking concept in SCAN [17] and its regularized version of r^2 SCAN [20], Liu and Shang [8] proposed a unified theory for both conventional and unconventional superconductors. Their work indicates that the SCC represents a symmetry-broken configuration, and DFT-predicted charge density changes can identify

superconductivity at 0 K. Furthermore, T_C can be estimated using the zentropy theory [21,22], which considers competition between the SCC and NCC. Using these ideas, 14 conventional superconductors were identified among 18 elements with A1, A4, A6, and A7 structures (Al, Pb, Cu, Ag, Au, Rh, Ir, Pd, Pt, *Ca*, *Sr*, *Si*, *Ge*, Sn, In, *As*, Sb, and Bi; where underlined italic elements are non-superconducting) and MgB₂ at 0 K and 0 GPa; along with one unconventional superconductor of YBCO₇ [8]. It is noted that in their work, they missed the more recent experimental observation that Bi is a superconductor with $T_C = 0.53$ mK at ambient pressure [22], which was pointed in private communications by Ramakrishnan, one of the authors of the publication. In those communications, Ramakrishnan also mentioned that they were not able to detect the superconductivity of Sb down to 0.1 mK and Au down to 0.05 mK, probably due to the slightly inferior Sb crystals with residual resistivity ratio of 200 as compared to above 600 for Bi and a few parts per million of Mn in Au.

The present work extends this verification by examining additional conventional superconductors at 0 K and 0 GPa. These include 12 hexagonal close-packed (hcp) elements (Be, Mg, Sc, Y, Ti, Zr, Hf, Tc, Re, Ru, Os, and Zn), 5 body-centered cubic (bcc) elements (V, Nb, Ta, Mo, and W), and the compound Nb₃Sn. These elements were chosen for their structural simplicity and available experimental data [23,24] (see Table 1), while Nb₃Sn was included because both its SCC and NCC have been experimentally characterized (Sec. 3.3). For each material, SCC and NCC were generated (Sec. 2.1), DFT-based calculations were performed (Sec. 2.2), and superconductivity was assessed based on predicted straight one-dimensional tunnels (SODTs). All examined materials exhibit superconductivity at 0 K and 0 GPa, including Mg, Sc, and Y, which remain experimentally unconfirmed under ambient conditions (see Sec. 3 and Table 1).

2 Methodology

2.1 Definition of superconducting configuration (SCC) at 0 K and 0 GPa

Our framework for examining superconductivity using DFT is inspired by several established concepts [8]: Cooper pairing via electron–phonon interactions in the BCS theory; the existence of a ground-state configuration at 0 K and 0 GPa with a unique electron density as described by

DFT; and the symmetry-broken configurations introduced by Gibbs [18,19] and later incorporated into meta-GGA functionals such as SCAN [17] and r^2 SCAN [20].

We define the superconducting configuration (SCC) as a symmetry-broken ground-state at 0 K and 0 GPa, formed through atomic perturbations of the normal conducting configuration (NCC), which dominates above T_C and exhibits higher symmetry. Both SCC and NCC charge densities, which represent the spatial distribution of electrons, can be predicted by DFT. We further propose that the SCC versus NCC charge density difference (SNCDD) form SODTs, acting as “superhighways” for electricity transportation without resistance, analogous to Cooper pairs transport in BCS theory. Electron-phonon interactions in this framework are embedded within DFT calculations of the SCC and NCC, represented by the applied atomic perturbations in SCC.

For practical implementation, materials studied via DFT can be grouped into two categories based on symmetry, which is experimentally measurable using techniques such as X-ray or neutron diffraction:

- Category-1: Higher-symmetry structures with fixed atomic positions (e.g., pure elements with bcc, fcc, and hcp structures, and Ni_3Sn with its A15 cubic structure [25,26]).
- Category-2: Lower-symmetry structures with variable atomic positions (e.g., high- T_C superconductors such as $\text{YBa}_2\text{Cu}_3\text{O}_{7-\delta}$ [27] and $\text{La}_{2-x}\text{Ba}_x\text{CuO}_4$ [28]).

For Category-1 materials, experimentally measured structures are treated as NCC. SCC is generated by randomly perturbing atomic positions [8],

$$(x_0 + n_x \delta_{ini}, \quad y_0 + n_y \delta_{ini}, \quad z_0 + n_z \delta_{ini}) \quad \text{Eq. 4}$$

where x_0, y_0, z_0 are atomic coordinates in the NCC; n_x, n_y , and n_z are random numbers 0, 1, or -1; and δ_{ini} typically ranges from 0.02 to 0.08 (fractional coordinates) to prevent atoms from reverting to their original high-symmetry positions. These perturbations aim to mimic strong electron-phonon interactions to identify stable SCCs and typically exceed those used in harmonic phonon and electron-phonon coupling calculations [29,30]. After testing multiple δ_{ini} values, the configuration yielding the lowest total energy is selected as the SCC. After performing DFT-based calculations, the atomic displacements between the SCC and NCC for each atom can be

expressed as,

$$(\Delta x, \Delta y, \Delta z).$$

Eq. 5

Correspondingly, the magnitude of the atomic movement is denoted by ΔR .

For Category-2 materials, experimentally measured structures are treated as the SCC, while the NCC is constructed by restoring symmetry. For example, in $\text{YBa}_2\text{Cu}_3\text{O}_7$, atoms in the Cu-O (x-y) plane can be adjusted to the same z level; see details in [8]. The present work focuses on Category-1 materials, which are typically conventional superconductors.

As a special case in the present work, Nb_3Sn ($T_c \approx 18$ K [25]) is unique because both the NCC (cubic) and SCC (tetragonal) phases have been experimentally observed (see Section 3.3). These measurements serve to validate our proposed approach for defining the NCC and SCC.

2.2 Details of DFT-based calculations for SCC and NCC

All DFT-based calculations in the present work were performed using the VASP code [31], with ion-electron interactions described by the projector augmented wave (PAW) method [32]. Two X-C functionals were employed: the widely used GGA developed by Perdew-Burke-Ernzerhof (PBE) [33] and the highly accurate meta-GGA functional, $r^2\text{SCAN}$ [17,34]. In all VASP calculations, electron configurations for each element follow those used by the Materials Project [35] and are listed in Table S1. Supercell sizes were set to $3 \times 3 \times 2$ (36 atoms) for hcp elements, $3 \times 3 \times 3$ (54 atoms) for bcc elements, and $2 \times 2 \times 2$ (64 atoms) for Nb_3Sn . The electronic self-consistency criterion was consistently set to 10^{-6} eV/atom, based on convergence tests from our previous work [8]. For pure elements, selected k -point meshes of $7 \times 7 \times 7$ were used, and energy cutoffs (E_{cut}) were determined by VASP with using PREC = High (specific values listed in Table S1).

In these calculations, structural relaxations were performed using the Methfessel-Paxton smearing [36] for at least three iterations and the charge density was computed using the tetrahedron method with a Blöchl correction [37]. Isosurface levels (F_{level}) for plotting the SCC-NCC charge density differences (SNCDDs) were chosen using VESTA [38] (see Table S1). F_{level}

was set near the maximum value that still produces connected SNCDDs; lower values would generate fully connected three-dimensional (3D) tunnels across the material. For Nb_3Sn , equilibrium properties of volume (V_0), bulk modulus (B_0) and its derivative with respect to pressure (B') were fitted using the four-parameter Birch-Murnaghan equation of state (EOS) [39] with inputs derived from the DFT energy-volume data.

Symmetry constraints were fully disabled in all VASP calculations involving pure elements to allow for spontaneous symmetry breaking in the SCCs. For Nb_3Sn , the cubic A15 phase is ferromagnetic, while the tetragonal phase is non-magnetic.

2.3 Identification of superconductor at 0 K and 0 GPa

A material is classified as a superconductor at 0 K and 0 GPa based on the following criteria [8]:

- 1) **Metallic nature:** Non-zero electronic DOS at the Fermi level, consistent with BCS theory (see Eq. 1).
- 2) **Ground-state SCC:** The SCC possesses lower energy than the NCC ($\Delta E_{SN} < 0$). This criterion is omitted in the present work because contemporary X-C functionals cannot reliably capture ΔE_{SN} , which is typically in the meV range and fall within DFT error margins.
- 3) **Formation of SODTs:** The SCC-NCC charge density difference (SNCDD) forms SODTs, serving as the primary indicator of superconductivity in this work. These SODTs result from regular, systematic atomic displacements between the SCC and NCC.

Thus, the key criteria adopted here are metallicity and the successful formation of SODTs, while the energy-based comparison is acknowledged but excluded due to current functional limitations.

3 Results and discussion

Table 1 summarizes the DFT-based results for identifying superconductivity of hcp elements (Be, Mg, Sc, Y, Ti, Zr, Hf, Tc, Re, Ru, Os, and Zn; see Sec. 3.1), bcc elements (V, Nb, Ta, Mo, and W; see Sec. 3.2), and Nb_3Sn (Sec. 3.3) at 0 K and 0 GPa, using the criteria defined in Sec. 2.3. Table

1 also details available experimental observations and provides a list of figures illustrating the predicted SNCDDs. Atomic displacements between the NCC and SCC for each material are compiled in Table S2, including the average movements obtained from the DFT calculations along with the mean atomic displacements defined in Eq. 5.

3.1 HCP metals

3.1.1 Be and Mg

Both alkaline earth metals, beryllium (Be) and magnesium (Mg), crystallize in the hcp structure at ambient pressure and low temperatures [40]. As an example, Figure S 1 (a and b) presents the total charge densities of Be with the NCC and SCC configurations as predicted by r^2 SCAN. The charge densities are nearly identical for both configurations, showing spherical shapes around each atom. However, Figure S 1 (c and d) illustrates the predicted SNCDDs of Be using r^2 SCAN, revealing SODTs along the *c*-axis for electrons and the *b*-axis for holes. By analyzing all atomic displacements defined in Eq. 5, we find that only two distinct displacement magnitudes occur, i.e., $\Delta R = 0.0481 \pm 6.6\text{E-}5 \text{ \AA}$ and $0.0256 \pm 2.0\text{E-}4 \text{ \AA}$ (see Table S2). The two values correspond to the Wyckoff-position sites (2c) of the hcp space group *P6₃/mmc*, located at $(\frac{1}{3}, \frac{2}{3}, \frac{1}{4})$ and $(\frac{2}{3}, \frac{1}{3}, \frac{3}{4})$. The extremely small standard deviations of these displacement magnitudes ($< 0.0002 \text{ \AA}$) indicate that the atomic shifts between the SCC and NCC are highly regular and systematic, ultimately giving rise to the formation of the SODTs.

Notably, the GGA functional predicts that both electron and hole SNCDDs exhibit SODTs along the *b*-axis. Table 1 summarizes the predicted energy difference between the SCC and NCC (ΔE_{SN} , cf. Eq. 3). The values are approximately zero (0.005 meV by GGA) and negative (-2.049 meV by r^2 SCAN), indicating a slight energetic preference for SCC. Based on the predicted SODTs, we conclude that Be is a superconductor at 0 K and 0 GPa. Experimentally, bulk Be has been observed to exhibit superconductivity at ambient pressure with an extremely low T_c of 26 mK [24,41], as evidenced by changes in magnetic susceptibility [41]. These experimental findings, along with the present DFT predictions, are summarized in Table 1.

Figure 1 shows the predicted SNCDDs of hcp Mg using GGA, which reveal charge density characteristics similar to those of hcp Be. Specifically, Mg exhibits SODTs along the *b*-axis for electrons and the *c*-axis for holes. In contrast, r^2 SCAN does not predict SODTs for hcp Mg (Figure S 2), instead showing a heavy zigzag SNCDD for electrons and a 3D character for holes.

By analyzing the atomic displacements of hcp Mg (see Eq. 5 and Table S2), the GGA-predicted ΔR values can be grouped into only two distinct displacement magnitudes, exhibiting extremely small standard deviations: $0.0420 \pm 6.5\text{E-}5$ Å and $0.0427 \pm 6.1\text{E-}4$ Å. These very small deviations indicate highly regular and systematic atomic shifts between the SCC and NCC, which in turn facilitate the formation of SODTs. In contrast, the r^2 SCAN-predicted ΔR values, grouped in the same manner as for the GGA case, display much larger standard deviations: 0.0426 ± 0.0178 Å and 0.0493 ± 0.0184 Å. This broad variation arises from irregular atomic displacements along the *z*-axis, where $\Delta z = -0.0004 \pm 0.0161$ Å and -0.0055 ± 0.0156 Å, with standard deviations far exceeding the corresponding mean values (see Table S2). Such irregular atomic displacements produce a strongly zigzag SNCDD, preventing the formation of SODTs.

Table 1 indicates that the predicted ΔE_{SN} values for Mg are close to zero (0.010 meV by GGA and -0.654 meV by r^2 SCAN). Based on the GGA-predicted SODTs, we conclude that Mg is a superconductor at 0 K and 0 GPa. Although superconductivity has not been experimentally observed in pure Mg at ambient pressure, evidence from Mg-rich Mg-Cd alloys suggests that pure Mg should be superconducting, with an extrapolated T_C around 0.5 mK [42]. Furthermore, Buhrman and Halperin [43] used the superconducting proximity effect to establish a new low upper bound of 2 mK for the transition temperature of Ag, Au, and Mg. These findings align with the present DFT predictions using GGA, as shown in Table 1.

3.1.2 Sc and Y

Both scandium (Sc) and yttrium (Y) are closely associated with the rare earth group and crystallize in the hcp structure at ambient pressure and low temperatures [40]. Figure S 3 illustrates the predicted SNCDDs of Sc using the r^2 SCAN functional, showing SODTs along the [110] direction. Table S2 shows that all atomic displacements of hcp Sc can be grouped into a

single, well-defined displacement magnitude with a small standard deviation ($\Delta R = 0.0444 \pm 0.0017 \text{ \AA}$). This narrow distribution indicates that the atomic shifts between the SCC and NCC are highly regular and systematic, thereby enabling the formation of SODTs. Table 1 shows that the predicted ΔE_{SN} value is close to zero (0.077 meV by GGA and -0.158 meV by $r^2\text{SCAN}$). Based on the $r^2\text{SCAN}$ -predicted SODTs (with GGA showing similar characteristics), we conclude that Sc is a superconductor at 0 K and 0 GPa. Experimentally, superconductivity has not been observed in Sc at ambient pressure, but it has been reported at high pressures, for example, T_c of 0.34 K at 21 GPa [23,24] and 36 K at 260 GPa [44]. These experimental observations, along with the present DFT results, are summarized in Table 1.

Figure S 4 presents the predicted SNCDDs of Y using $r^2\text{SCAN}$, which are similar to those of Sc, showing SODTs along the b -axis direction for both electron and hole SNCDDs. Similar to the case of hcp Sc, Table S2 shows that hcp Y exhibits a single, well-defined displacement magnitude with a small standard deviation ($\Delta R = 0.0591 \pm 6.0\text{E-}4 \text{ \AA}$), indicating that its atomic shifts are sufficiently regular to support the formation of SODTs. Table 1 indicates that the predicted ΔE_{SN} values are also close to zero (-0.0097 meV by GGA and 0.0292 meV by $r^2\text{SCAN}$). Based on the $r^2\text{SCAN}$ predictions (with GGA yielding similar results), we conclude that Y is a superconductor at 0 K and 0 GPa. Similar to Sc, superconductivity in Y has not been observed at ambient pressure above 6 mK [45]. However, it has been detected under high pressures, for example, T_c of 0.34 K at 21 GPa [23,24], 17 K at 89 GPa [45], and 20 K at 115 GPa [46]. These experimental findings and the present DFT predictions for Y are summarized in Table 1.

3.1.3 Ti, Zr, and Hf

The early transition metals titanium (Ti), zirconium (Zr), and hafnium (Hf) belong to the same group on the periodic table, and crystallize in the hcp structure at ambient pressure and low temperatures [40]. Figure S 5 illustrates the predicted SNCDDs of hcp Ti predicted using $r^2\text{SCAN}$, showing SODTs along the c -axis direction for both electron and hole SNCDDs. The GGA functional predicts similar characteristics. Table 1 shows that the predicted ΔE_{SN} is slightly positive (0.012 meV by GGA and 0.039 meV by $r^2\text{SCAN}$). Based on these predicted SODTs, we conclude that Ti is a superconductor at 0 K and 0 GPa. Experimentally, Ti has been confirmed as

a conventional Type I superconductor at ambient pressure, with a T_C of approximately 0.5 K [23,24]. These observations are consistent with the present DFT predictions, and the results are summarized in Table 1.

The predicted SNCDDs of hcp Zr and hcp Hf using r^2 SCAN are shown in Figure S 6 and Figure S 7, respectively. Both elements exhibit similar charge density characteristics, displaying SODTs along the *b*-axis direction for both electron and hole SNCDDs. Table 1 shows that the predicted ΔE_{SN} values are close to zero: slightly negative for Zr (-0.00003 meV) and slightly positive for Hf (0.036 meV) by r^2 SCAN. Based on these predicted SODTs, we conclude that Zr and Hf are superconductors at 0 K and 0 GPa. Experimentally, superconductivity in Zr and Hf has been confirmed at ambient pressure using magnetic threshold curves measurements [47], with T_C of 0.6 K for Zr and 0.38 K for Hf [23,24]. These findings agree with the present DFT predictions using both GGA and r^2 SCAN and are summarized in Table 1.

Note that the formation of SODTs in hcp Ti, Zr, and Hf arises from a single, well-defined displacement magnitude with a small standard deviation for each element ($\Delta R = 0.0978 \pm 7.8E-4$ Å, $0.0524 \pm 1.9E-4$ Å and $0.0514 \pm 4.0E-4$ Å, respectively; see Table S2). These narrow distributions demonstrate that the atomic shifts between the SCC and NCC are highly regular and systematic, thereby supporting the formation of SODTs in Ti, Zr, and Hf.

3.1.4 T_c , Re, Ru, and Os

Technetium (T_c) is the lightest element without any stable isotopes and crystallizes in an hcp structure. Despite its radioactivity, its superconducting properties have been well-characterized, exhibiting ambient-pressure superconductivity with a relatively high critical temperature ($T_C = 8.2$ K [23,24]). Unlike Type I superconductors such as Ti and Zr, T_c is a Type II superconductor, allowing partial magnetic field penetration via quantized vortices. Figure S 8 shows the predicted SNCDDs of hcp T_c using r^2 SCAN, revealing SODTs along the [110] direction formed by connecting ellipsoidal charge densities. Table 1 indicates slightly negative values for the predicted ΔE_{SN} (-0.020 meV by GGA and -0.028 meV by r^2 SCAN). Based on the predicted SODTs, we conclude that hcp T_c is a superconductor at 0 K and 0 GPa, consistent with

experimental observations [23,24]. Table 1 summarizes the present DFT predictions (using both GGA and r^2 SCAN) and experimental findings for hcp Tc.

Figure S 9 presents the predicted SNCDDs of hcp rhenium (Re) using both GGA and r^2 SCAN. Only the hole SNCDD by GGA shows SODT along the *b*-axis direction, while no clear SODTs are observed in other predictions. Table 1 shows slightly negative ΔE_{SN} values (-0.014 meV by GGA and -0.35 meV by r^2 SCAN). Based on the GGA-predicted SODTs, we conclude that hcp Re is a superconductor at 0 K and 0 GPa. Experimentally, pure Re is a conventional Type I superconductor at ambient pressure with a measured T_c of 1.7 K [23,24], which agrees with the present DFT predictions. These results are summarized in Table 1.

Figure S 10 illustrates the predicted electron and hole SNCDDs of hcp ruthenium (Ru) by r^2 SCAN, showing SODTs along the *c*-axis direction. Although the charge density exhibits weak zigzag characteristics, these features do not disrupt the SODTs (similar features are seen in Os and Zn). Table 1 shows that the predicted ΔE_{SN} values are slightly negative (-0.014 meV by GGA and -0.012 meV by r^2 SCAN). Based on the r^2 SCAN-predicted SODTs (with GGA yielding similar results), we conclude that hcp Ru is a superconductor at 0 K and 0 GPa. Experimentally, pure Ru is a conventional Type I superconductor at ambient pressure with a measured T_c of 0.5 K [23,24]. Experimental findings agree with the present DFT predictions, and these results are summarized in Table 1.

Figure S 11 shows the predicted SNCDDs of hcp osmium (Os) using r^2 SCAN, revealing SODTs along the *b*-axis direction with slight zigzag features for both electron and hole distributions. Table 1 shows slightly positive ΔE_{SN} values (0.0189 meV by GGA and 0.1611 meV by r^2 SCAN). Based on the r^2 SCAN-predicted SODTs (with GGA showing similar results), we conclude that hcp Os is a superconductor at 0 K and 0 GPa, consistent with experimental observations. Pure Os is a conventional Type I superconductor at ambient pressure with a measured T_c of 0.7 K [23,24]. These calculated and measured results are summarized in Table 1.

Consistent with the above analyses, the formation of SODTs in hcp Tc, Ru, and Os obtained using r^2 SCAN and hcp Re obtained using GGA (instead of r^2 SCAN), arises from highly regular

and systematic atomic shifts between the SCC and NCC (see Table S2). These well-ordered displacements support the formation of SODTs in Tc, Ru, and Os (r^2 SCAN) and in Re (GGA).

In contrast, for hcp Re calculated using r^2 SCAN, which mirrors the behavior observed for hcp Mg with r^2 SCAN, the atomic shifts between the SCC and NCC are irregular, with $\Delta R = 0.0447 \pm 0.0498 \text{ \AA}$ and 0.0447 ± 0.0108 (see Table S2). The large standard deviations relative to the mean values indicate pronounced structural disorder, which prevents the formation of SODTs in hcp Re under r^2 SCAN.

3.1.5 Zn

Zinc (Zn) crystallizes in the hcp structure at ambient pressure and low temperatures [40]. Figure S 12 illustrates the predicted electron and hole SNCDDs of hcp Zn using r^2 SCAN, showing the SODTs forming along the *c*-axis for electrons and the *b*-axis for holes due to the highly regular and systematic atomic shifts between the SCC and NCC ($\Delta R = 0.0449 \pm 1.0\text{E-}4 \text{ \AA}$ and $0.0330 \pm 6.6\text{E-}4 \text{ \AA}$, see Table S2). Table 1 presents the predicted ΔE_{SN} values of hcp Zn, which are close to zero (0.0742 meV by GGA and -1.791 meV by r^2 SCAN). Based on the r^2 SCAN-predicted SODTs (with GGA yielding similar results), we conclude that hcp Zn is a superconductor at 0 K and 0 GPa. Experimentally, pure Zn is a conventional Type I superconductor at ambient pressure with a measured T_c of 0.85 K [23,24]. These theoretical predictions and experimental observations are summarized in Table 1.

3.2 BCC metals: V, Nb, Ta, Mo, and W

The refractory metals vanadium (V), niobium (Nb), tantalum (Ta), molybdenum (Mo), and tungsten (W) all crystallize in a bcc structure at ambient pressure and low temperatures [40]. At ambient pressure, they are all conventional superconductors, classified as either Type I (e.g., Ta, Mo, and W) or Type II (e.g., V and Nb) [23,24]. Among these five elements, Nb exhibits the highest T_c temperature at ambient pressure (9.25 K), which is the highest among all pure elements [23,24], cf. Table 1. The other elements have lower T_c temperatures: 5.4 K for V, 4.4 K for Ta, 0.92 K for Mo, and 0.01 K for W [23,24] (see Table 1).

Figure 2 presents the r^2 SCAN-predicted electron and hole SNCDDs of bcc V, revealing clear SODTs along [111] for both electrons and holes. By analyzing the atomic displacements of bcc V (see Eq. 5), we find that all atoms exhibit a single, well-defined displacement vector (Table S2):

$$(\Delta x, \Delta y, \Delta z) = (0.0398 \pm 2.7\text{E-}4 \text{ \AA}, -0.0133 \pm 1.8\text{E-}4 \text{ \AA}, -0.0067 \pm 1.7\text{E-}4 \text{ \AA}), \quad Eq. 6$$

with a corresponding magnitude $\Delta R = 0.0425 \pm 3.6\text{E-}4 \text{ \AA}$. The extremely small standard deviations (on the order of 1E-4 \AA) indicate that the atomic shifts between the SCC and NCC are highly regular and systematic, thereby enabling the formation of the SODTs. Note that all other bcc elements examined (Nb, Ta, Mo, and W) exhibit similarly regular atomic displacements (Table S2).

In addition, GGA predicts similar charge density features, including SODTs along [111] of bcc V, see Figure S 13. Table 1 shows that the predicted ΔE_{SN} values are close to zero (0.024 meV by GGA and -1.561 meV by r^2 SCAN). Based on these predicted SODTs (using both r^2 SCAN and GGA), we conclude that bcc V is a superconductor at 0 K and 0 GPa, consistent with experimental observations ($T_c = 5.4 \text{ K}$ [23,24]).

Similar to bcc V, the other refractory metals Nb, Ta, Mo, and W exhibit comparable SNCDDs, as shown in Figure S 14, Figure S 15, Figure S 16, and Figure S 17, respectively, based on r^2 SCAN predictions (with GGA yielding similar results). All these SNCDDs exhibit SODTs along [111] for both electrons and holes, arising from the highly regular and systematic atomic shifts between the SCC and NCC (Table S2). Table 1 shows that the predicted ΔE_{SN} values are close to zero ($|\Delta E_{SN}| < 0.06 \text{ meV}$ for both GGA and r^2 SCAN). Based on these predicted SODTs, we conclude that the bcc Nb, Ta, Mo, and W are superconductor at 0 K and 0 GPa, in agreement with experimental observations [23,24]. All theoretical and experimental results are summarized in Table 1.

3.3 Nb_3Sn

Niobium-tin (Nb_3Sn), a member of A15 family of superconductors, crystallizing in a cubic structure with space group $Pm\bar{3}n$ (no. 223) [25,26]. At approximately 43 K, it undergoes a displacive martensitic transformation from the high-temperature cubic phase to a low-

temperature tetragonal phase with space group $P4_2/mmc$ (no. 131) [48–50]. This transformation is driven by a Jahn-Teller distortion [49].

Figure 3a shows the relaxed tetragonal configuration at 0 K predicted by GGA, with Sn atoms at Wyckoff site 2c (0, 0.5, 0), Nb1 atoms at 2e (0, 0, 0.25), and Nb2 atoms at 4k ($0.25-\delta$, 0.5, 0.5). Experimentally, the lattice parameter ratio a_0/c_0 changes from 1 to 1.0062 [50], closely matching the GGA prediction of 1.0087 (see Table 2). The Nb2 atomic displacement $|\delta|$ increases from 0 to 0.0031 at 4 K experimentally [50], compared to 0.0052 predicted by GGA. Below 18 K, tetragonal Nb_3Sn becomes superconducting [25]. These observations suggest that superconductivity in Nb_3Sn at low temperatures originates from a structural transformation from the high-temperature cubic phase ($T > 43$ K) to the low-temperature tetragonal phase, where the SCC dominates. This behavior is analogous to $BaFe_2As_2$, where a previous zentropy-based study showed that superconductivity emerges in the low-temperature antiferromagnetic (AFM) spin-density-wave (SDW) phase, with a thermal population of the SDW-AFM configuration exceeding 99.99% [51]. Since superconductivity is fragile and can be suppressed by exceeding any critical parameters, such as T_c , magnetic field, or current density, a dominant SCC is essential [52,53].

Figure 3b illustrates the energy versus volume ($E-V$) curves of cubic nonmagnetic (NM) and ferromagnetic (FM) configurations, and the tetragonal NM configuration of Nb_3Sn , calculated using GGA. The tetragonal FM configuration relaxes to the NM configuration, while the cubic FM phase exhibits an average magnetic moment of $0.106 \mu_B/\text{atom}$ at equilibrium volume. Figure 3b indicates that the ground state of Nb_3Sn is the tetragonal NM configuration with a predicted $\Delta E_{SN} = -0.392 \text{ meV/atom}$ with respect to the cubic FM configuration (Table 2).

Table 2 summarizes the crystallographic and structural properties of both cubic and tetragonal Nb_3Sn predicted by GGA, showing good agreement with experimental data, including equilibrium volume (V_0), a_0/c_0 ratio, and bulk modulus (B_0) [48,54]. Unlike the elemental cases discussed earlier, the high-temperature cubic A15 phase is considered as the NCC, while the low-temperature tetragonal phase is SCC for Nb_3Sn . Figure 4 shows the predicted electron and hole SNCDDs of Nb_3Sn using GGA. The electron SNCDDs exhibit distinct SODTs along the c -axis

(Figure 4a), arising from the highly regular and systematic atomic shifts between the experimental SCC and experimental NCC (whose standard derivations are set to zero for these experimental configurations, see Table S2), despite the Nb₂ atomic displacements occurring along the *a*- and *b*-axes (Figure 3a).

In contrast, the hole SNCDDs form a 3D network rather than SODTs. Based on the predicted electron SODTs, negative ΔE_{SN} , and metallic nature (absence of bandgap), we conclude that tetragonal Nb₃Sn is a superconductor at 0 K and 0 GPa, due primarily to electron transport along the *c*-axis. These findings are summarized in Table 1, align with experimental observations that tetragonal Nb₃Sn becomes superconducting below $T_c \approx 18$ K [25]. In the tetragonal phase, superconducting behavior is complex and no preferred crystallographic direction has been experimentally identified [55].

4 Summary

The present work verifies a recently proposed unified theoretical framework for superconductivity applicable to both conventional and unconventional materials [8]. The theoretical framework suggests that superconductivity originates from the formation of a *symmetry-broken* superconducting configuration (SCC), created by atomic perturbations of the normal conducting configuration (NCC). This transformation, driven by electron-phonon interactions, results in straight one-dimensional tunnels (SODTs) in the charge density difference, arising from the highly regular and systematic atomic shifts between the SCC and NCC. The verification is through DFT-based calculations at 0 K and 0 GPa for 12 hcp elements (Be, Mg, Sc, Y, Ti, Zr, Hf, Tc, Re, Ru, Os, and Zn), 5 bcc elements (V, Nb, Ta, Mo, and W); and one compound Nb₃Sn. Our results indicate that all these materials exhibit SODTs, supporting their superconducting nature at 0 K and 0 GPa. However, the superconductivity of Mg, Sc, and Y remain to be confirmed by experiments.

Current DFT calculations face limitations in accurately resolving the energy difference (ΔE_{SN}) between the SCC and NCC due to approximations in X-C functionals, highlighting the need for further methodological improvements. Once the SCC is identified for a given material, its

superconducting transition temperature (T_C) may be estimated by analyzing the competition between the SCC and NCC. This can be achieved using frameworks such as zentropy theory [21,22,56], which employs coarse-graining of entropy spanning multiple scales from macroscopic observations down to quantum-level fluctuations.

5 Acknowledgements

This work was supported by the U.S. Department of Energy (DOE) through Grant No. DE-SC0023185. First-principles calculations were performed partially on the Roar supercomputers at the PSU's Institute for Computational and Data Sciences (ICDS), partially on the resources of the National Energy Research Scientific Computing Center (NERSC), a DOE Office of Science User Facility supported under Contract No. DE-AC02-05CH11231 using the NERSC award BES-ERCAP0032760, and partially on the resources of Advanced Cyberinfrastructure Coordination Ecosystem: Services & Support (ACCESS) through allocation DMR1400063, which is supported by U.S. National Science Foundation Grants Nos. 2138259, 2138286, 2138307, 2137603, and 2138296.

6 Data availability statement

All data and plots that support the findings of the present work are included within this article and its supplementary files.

7 ORCID IDs

Zi-Kui Liu <https://orcid.org/0000-0003-3346-3696>

Shun-Li Shang <https://orcid.org/0000-0002-6524-8897>

8 Tables and Table Captions

Table 1. DFT-based predictions for superconductivity and related properties of pure elements and compounds: Superconductivity (Y for Yes, N for No), electrical conductivity (Cond: Y for conductor, N for nonconductor), whether SCC is the ground state (GS: Y or N), the energy difference between SCC and NCC (ΔE_{SN} in meV/atom), the morphology of the SCC-NCC charge density difference (SNCDD), and the predicted versus experimental superconductivity (Y_0 at zero pressure and Y_h at high pressure).

Mater.	X-C	DFT results			Characteristics of SNCDD by DFT	Superconductivity		Figures
		Cond	GS	ΔE_{SN}		Calc. ^a	Expt. ^b	
Be	GGA	Y	N	0.005	SODT along <i>c</i> - or <i>b</i> -axis.	Y_0	Y_0 (Type I) 26 mK	Figure S 1
	r ² SCAN	Y	Y	-2.049				
Mg	GGA	Y	N	0.010	SODT along <i>c</i> - or <i>b</i> -axis by GGA (zigzag electron by r ² SCAN, hole 3D)	Y_0	0.5 mK ^c 2 mK ^d	Figure 1 Figure S 2
	r ² SCAN	Y	Y	-0.654				
Sc	GGA	Y	N	0.077	SODT along [110]	Y_0	Y_h 0.34 K at 21 GPa	Figure S 3
	r ² SCAN	Y	Y	-0.158				
Y	GGA	Y	Y	-0.0097	SODT along <i>b</i> -axis.	Y_0	Y_h 2.8 K at 15 GPa	Figure S 4
	r ² SCAN	Y	N	0.0292				
Ti	GGA	Y	N	0.012	SODT along <i>c</i> -axis.	Y_0	Y_0 (Type I) 0.5 K	Figure S 5
	r ² SCAN	Y	N	0.039				
Zr	GGA	Y	Y	-0.0006	SODT along <i>b</i> -axis.	Y_0	Y_0 (Type I) 0.6 K	Figure S 6
	r ² SCAN	Y	Y	-0.00003				
Hf	GGA	Y	N	0.010	SODT along <i>b</i> -axis.	Y_0	Y_0 (Type I) 0.38 K	Figure S 7
	r ² SCAN	Y	N	0.036				
Tc	GGA	Y	Y	-0.020	SODT along [110]	Y_0	Y_0 (Type II) 8.2 K	Figure S 8
	r ² SCAN	Y	Y	-0.028				
Re	GGA	Y	Y	-0.014	SODT along <i>b</i> -axis by GGA	Y_0	Y_0 (Type I) 1.7 K	Figure S 9
	r ² SCAN	Y	Y	-0.35				
Ru	GGA	Y	Y	-0.014	SODT along <i>c</i> -axis (with zigzag character).	Y_0	Y_0 (Type I) 0.5 K	Figure S 10
	r ² SCAN	Y	Y	-0.012				
Os	GGA	Y	N	0.0189	SODT along <i>b</i> -axis.	Y_0	Y_0 (Type I) 0.7 K	Figure S 11
	r ² SCAN	Y	N	0.1611				
Zn	GGA	Y	N	0.0742	SODT along <i>c</i> - or <i>b</i> -axis.	Y_0	Y_0 (Type I) 0.85 K	Figure S 12
	r ² SCAN	Y	Y	-1.791				
V	GGA	Y	N	0.024	SODT along [111]	Y_0	Y_0 (Type II) 5.4 K	Figure S 13 Figure 2
	r ² SCAN	Y	Y	-1.561				
Nb	GGA	Y	Y	-0.009	SODT along [1̄1̄1]	Y_0	Y_0 (Type II) 9.25 K	Figure S 14
	r ² SCAN	Y	N	0.056				
Ta	GGA	Y	Y	-0.009	SODT along [111]	Y_0	Y_0 (Type I) 4.4 K	Figure S 15
	r ² SCAN	Y	Y	-0.039				
Mo	GGA	Y	N	0.003	SODT along [1̄1̄1]	Y_0	Y_0 (Type I) 0.92 K	Figure S 16
	r ² SCAN	Y	N	0.030				
W	GGA	Y	Y	-0.009	SODT along [111]	Y_0	Y_0 (Type I) 0.01 K	Figure S 17
	r ² SCAN	Y	Y	-0.002				
Nb ₃ Sn	GGA	Y	Y	-0.392	SODT along <i>c</i> -axis for electrons.	Y_0	Y_0 (Type II) 17.9 K	Figure 4
	r ² SCAN	Y	Y	-1.003				

^a This work with Y_0 for superconductor at zero pressure.

^b Experimentally observed superconducting elements at ambient pressure (marked by Y_0) or high pressure (marked by Y_h), and the values indicate the measured T_c for pure elements [23,24] and Nb₃Sn [25].

^c Extrapolation from the data on Mg-rich alloys gives a value of $T_c = 0.5$ mK for pure magnesium [42].

^d Using the proximity effect, the established a new upper bound of 2 mK for the transition temperature of Ag, Au, and most importantly Mg [43].

Table 2. Crystallographic and structural properties of cubic and tetragonal Nb_3Sn by DFT-based calculations using GGA in comparison with experiments.

Note	E_0 (meV/atom)	V_0 ($\text{\AA}^3/\text{atom}$)	a_0/c_0	B_0 (GPa)	B'	MM (μ_B/atom)
DFT, cubic (FM)	0.000	18.961	1	163.5	4.27	0.106
DFT, cubic (NM)	0.262	18.958	1	163.6	4.29	0
DFT, tet (NM)	-0.392	18.964	1.0087	163.3	4.33	0
Expt., cubic		18.42 ^a	1	165 ^b		
Expt., tet		18.43 ^a	1.0061 ^a	161 ^b		

^a Measured at 5.1 K for tetragonal phase and 50 K for cubic phase [48].

^b Used by Lu and Klein [54].

9 Figures and Captions (main)

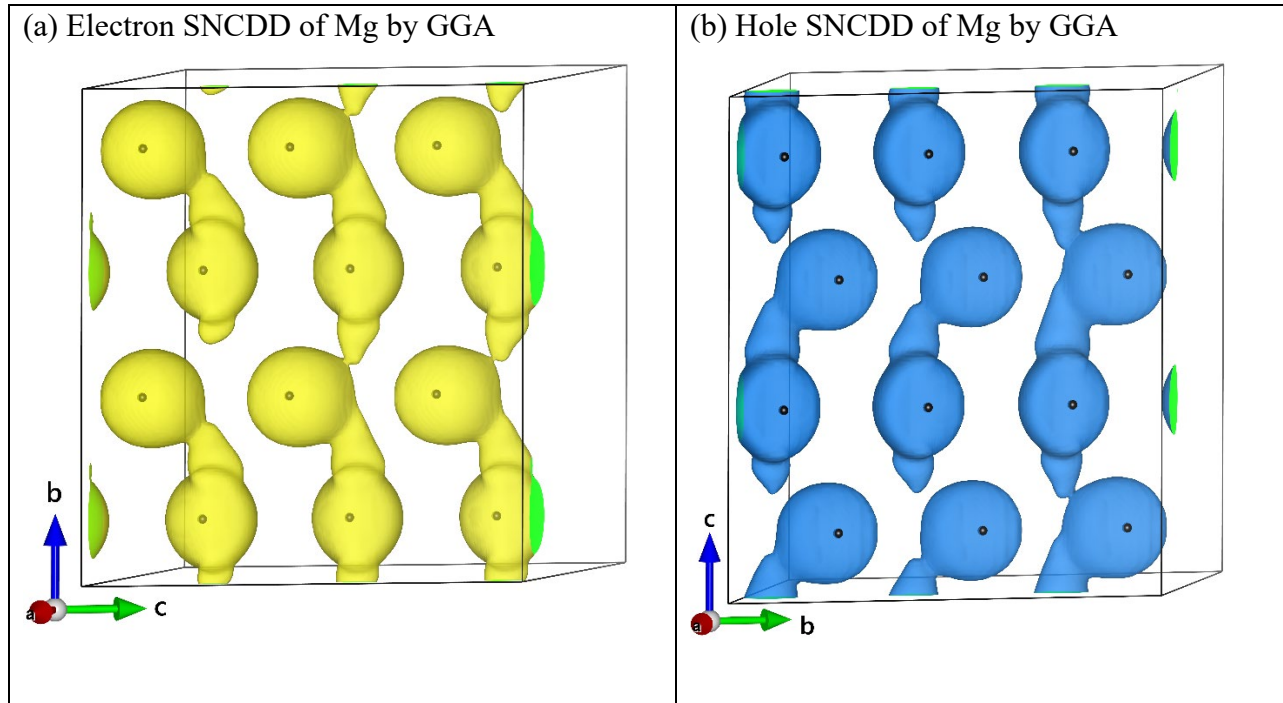
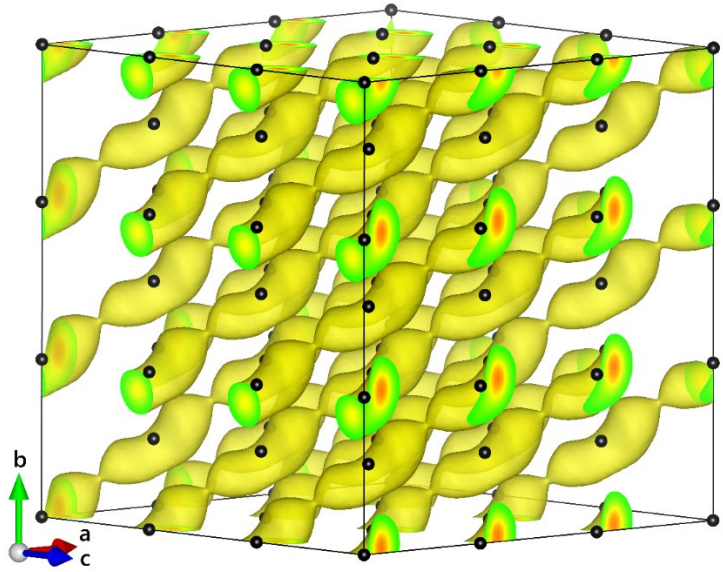


Figure 1. Partial electron (a, yellow) and hole (b, blue) SNCDDs of Mg predicted by GGA-PBE, showing SODTs along the b-axis for electron and along the c-axis for hole SNCDD. In contrast, r^2 SCAN does not exhibit SODTs for Mg, see Figure S 2.

(a) Electron SNCDD of V by r^2 SCAN



(b) Hole SNCDD of V by r^2 SCAN

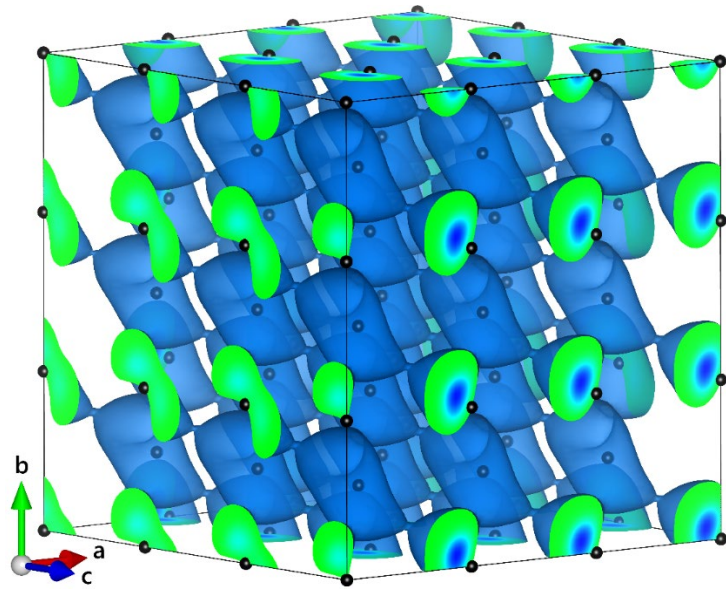


Figure 2. Electron (a, yellow) and hole (b, blue) SNCDDs of V predicted by r^2 SCAN, showing SODTs along [111]. For comparison, predictions by GGA-PBE are provided in Figure S 13.

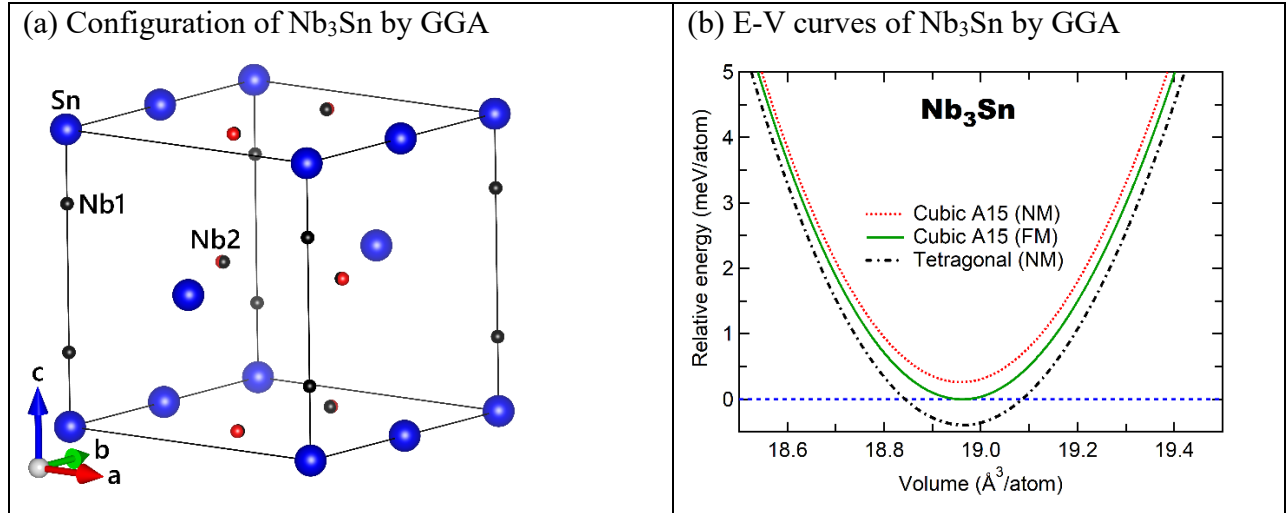


Figure 3. Relaxed crystal configuration (a) and the predicted energy-volume (E-V) curves for Nb_3Sn using GGA-PBE. For the tetragonal Nb_3Sn , the Nb_2 atoms (red plus black) at Wyckoff site $4m$ ($0.25-\delta, 0.25, 0$) exhibit a displacement $|\delta|$ around 0.0043 according to GGA predictions, compared to the measured $|\delta| = 0.0031$ at 4 K [50].

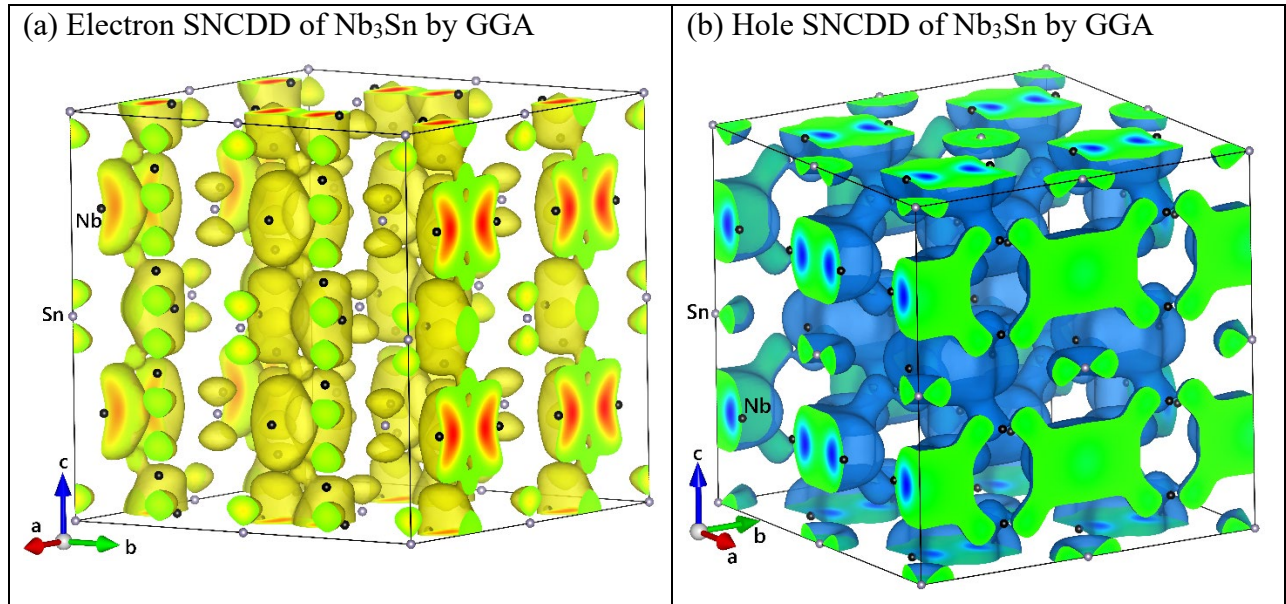


Figure 4. Electron (a, yellow) and hole (b, blue) SNCDDs of Nb_3Sn predicted by GGA-PBE, showing SODTs along the c -axis for electron, while no SODTs for hole.

10 References

- [1] Kamerlingh Onnes H 1911 Further experiments with liquid helium. C. On the change of electric resistance of pure metals at very low temperatures etc. IV. The resistance of pure mercury at helium temperatures *K. Ned. Akad. van Wet. Proc.* **13** (2) 1274–6
- [2] Bardeen J, Cooper L N and Schrieffer J R 1957 Theory of Superconductivity *Phys. Rev.* **108** 1175–204
- [3] McMillan W L 1968 Transition temperature of strong-coupled superconductors *Phys. Rev.* **167** 331–44
- [4] Pickard C J, Errea I and Eremets M I 2020 Superconducting Hydrides Under Pressure *Annu. Rev. Condens. Matter Phys.* **11** 57–76
- [5] Giustino F 2017 Electron-phonon interactions from first principles *Rev. Mod. Phys.* **89** 015003
- [6] Karsai F, Engel M, Flage-Larsen E and Kresse G 2018 Electron–phonon coupling in semiconductors within the GW approximation *New J. Phys.* **20** 123008
- [7] Sadovskii M V. 2025 Upper limit for superconducting transition temperature in electron-phonon superconductors: very strong coupling *arXiv: 2506.19326*
- [8] Liu Z-K and Shang S-L 2025 Revealing symmetry-broken superconducting configurations by density functional theory *Supercond. Sci. Technol.* **38** 075021
- [9] Tinkham M 2004 *Introduction to Superconductivity: Second Edition*
- [10] Mangin P and Kahn R 2017 *Superconductivity: An introduction* (Cham: Springer International Publishing)
- [11] Xing J, Li S, Zeng B, Mu G, Shen B, Schneeloch J, Zhong R D, Liu T S, Gu G D and Wen H-H 2014 Power-law-like correlation between condensation energy and superconducting transition temperatures in iron pnictide/chalcogenide superconductors: Beyond the BCS understanding *Phys. Rev. B* **89** 140503
- [12] Ortega J, Zúñiga F and de Llano M 2020 Condensation Energy in a Superconductor for All Temperatures *J. Low Temp. Phys.* **201** 489–99
- [13] Hohenberg P and Kohn W 1964 Inhomogeneous Electron Gas *Phys. Rev.* **136** B864–71
- [14] Kohn W and Sham L J 1965 Self-consistent equations including exchange and correlation effects *Phys. Rev.* **140** A1133–8
- [15] Giustino F 2017 Electron-phonon interactions from first principles *Rev. Mod. Phys.* **89**

- [16] Aouina A, Borlido P, Marques M A L and Botti S 2024 Assessing Exchange-Correlation Functionals for Accurate Densities of Solids *J. Chem. Theory Comput.* **20** 10852–60
- [17] Sun J, Ruzsinszky A and Perdew J 2015 Strongly constrained and appropriately normed semilocal density functional *Phys. Rev. Lett.* **115** 036402
- [18] Gibbs J W 1902 *Elementary Principles in Statistical Mechanics: Developed with Especial Reference to the Rational Foundation of Thermodynamics* (New York: Charles Scribner's Sons)
- [19] Gibbs J W 1948 *The collected works of J. Willard Gibbs: Vol. II Elementary Principles in Statistical Mechanics* (New Haven: Yale University Press, Vol. II)
- [20] Furness J W, Kaplan A D, Ning J, Perdew J P and Sun J 2020 Accurate and numerically efficient r2SCAN meta-generalized gradient approximation *J. Phys. Chem. Lett.* **11** 8208–15
- [21] Liu Z-K, Wang Y and Shang S-L 2022 Zentropy theory for positive and negative thermal expansion *J. Phase Equilibria Diffus.* **43** 598–605
- [22] Liu Z-K 2024 Quantitative predictive theories through integrating quantum, statistical, equilibrium, and nonequilibrium thermodynamics *J. Phys. Condens. Matter* **36** 343003
- [23] Grochala W 2003 Web Site: Following the Link of the Least Resistance *Angew. Chemie Int. Ed.* **42** 1682–1682
- [24] Buzea C and Robbie K 2005 Assembling the puzzle of superconducting elements: a review *Supercond. Sci. Technol.* **18** R1–8
- [25] Stewart G R 2015 Superconductivity in the A15 structure *Phys. C Supercond. its Appl.* **514** 28–35
- [26] Koblischka M R, Roth S, Koblischka-Veneva A, Karwoth T, Wiederhold A, Zeng X L, Fasoulas S and Murakami M 2020 Relation between Crystal Structure and Transition Temperature of Superconducting Metals and Alloys *Met. 2020, Vol. 10, Page 158* **10** 158
- [27] Williams A, Kwei G H, Von Dreele R B, Raistrick I D and Bish D L 1988 Joint x-ray and neutron refinement of the structure of superconducting $\text{YBa}_2\text{Cu}_3\text{O}_7\text{-}x$: Precision structure, anisotropic thermal parameters, strain, and cation disorder *Phys. Rev. B* **37** 7960–2
- [28] Katano S, Fernandez-Baca J A, Funahashi S, Môri N, Ueda Y and Koga K 1993 Crystal structure and superconductivity of $\text{La}_{2-x}\text{Ba}_x\text{CuO}_4$ ($0.03 \leq x \leq 0.24$) *Phys. C Supercond.*

- [29] Zacharias M and Giustino F 2020 Theory of the special displacement method for electronic structure calculations at finite temperature *Phys. Rev. Res.* **2** 013357
- [30] Sun Y, Zhang F, Wang C Z, Ho K M, Mazin I I and Antropov V 2022 Electron-phonon coupling strength from ab initio frozen-phonon approach *Phys. Rev. Mater.* **6** 074801
- [31] Kresse G and Furthmüller J 1996 Efficient iterative schemes for *ab initio* total-energy calculations using a plane-wave basis set *Phys. Rev. B* **54** 11169–86
- [32] Kresse G, Joubert D, Kresse D and Joubert G 1999 From ultrasoft pseudopotentials to the projector augmented-wave method *Phys. Rev. B* **59** 1758–75
- [33] Perdew J P, Burke K and Ernzerhof M 1996 Generalized gradient approximation made simple *Phys. Rev. Lett.* **77** 3865–8
- [34] Kothakonda M, Kaplan A D, Isaacs E B, Bartel C J, Furness J W, Ning J, Wolverton C, Perdew J P and Sun J 2023 Testing the r2SCAN density functional for the thermodynamic stability of solids with and without a van der Waals correction *ACS Mater. Au* **3** 102–11
- [35] Jain A, Ong S P, Hautier G, Chen W, Richards W D, Dacek S, Cholia S, Gunter D, Skinner D, Ceder G and Persson K A 2013 Commentary: The Materials Project: A materials genome approach to accelerating materials innovation *APL Mater.* **1** 011002
- [36] Methfessel M and Paxton A T 1989 High-precision sampling for Brillouin-zone integration in metals *Phys. Rev. B* **40** 3616–21
- [37] Blöchl P E, Jepsen O and Andersen O K 1994 Improved tetrahedron method for Brillouin-zone integrations *Phys. Rev. B* **49** 16223–33
- [38] Momma K and Izumi F 2011 VESTA3 for three-dimensional visualization of crystal, volumetric and morphology data *J. Appl. Crystallogr.* **44** 1272–6
- [39] Shang S-L, Wang Y, Kim D and Liu Z-K 2010 First-principles thermodynamics from phonon and Debye model: Application to Ni and Ni₃Al *Comput. Mater. Sci.* **47** 1040–8
- [40] Tonkov E Y and Ponyatovsky E G 2005 *Phase transformations of elements under high pressure* (CRC Press)
- [41] Falge R L 1967 Superconductivity of hexagonal beryllium *Phys. Lett. A* **24** 579–80
- [42] Mota A C, Brewster P and Wang R 1972 Superconductivity in the Mg–Cd system: Extrapolated T_c for pure magnesium *Phys. Lett. A* **41** 99–101
- [43] Buhrman R A and Halperin W P 1974 The elimination of supercooling in

superconductors by the proximity effect: New bounds on Tc for Mg, Ag, and Au *J. Low Temp. Phys.* **16** 409–15

- [44] Ying J, Liu S, Lu Q, Wen X, Gui Z, Zhang Y, Wang X, Sun J and Chen X 2023 Record High 36 K Transition Temperature to the Superconducting State of Elemental Scandium at a Pressure of 260 GPa *Phys. Rev. Lett.* **130** 256002
- [45] Hamlin J J, Tissen V G and Schilling J S 2006 Superconductivity at 17 K in yttrium metal under nearly hydrostatic pressures up to 89 GPa *Phys. Rev. B* **73** 094522
- [46] Hamlin J J, Tissen V G and Schilling J S 2007 Superconductivity at 20 K in yttrium metal at pressures exceeding 1Mbar *Phys. C Supercond. its Appl.* **451** 82–5
- [47] Smith T S and Daunt J G 1952 Some Properties of Superconductors below 1°K. III. Zr, Hf, Cd, and Ti *Phys. Rev.* **88** 1172–6
- [48] Mailfert R, Batterman B W and Hanak J J 1969 Observations related to the order of the low temperature structural transformation in V3Si and Nb3Sn *Phys. status solidi* **32** K67–9
- [49] Kragler R 1978 Behavior of the elastic moduli of Nb3Sn in the low temperature phase *Phys. B+C* **93** 314–26
- [50] Shirane G and Axe J D 1971 Neutron scattering study of the lattice-dynamical phase transition in Nb3Sn *Phys. Rev. B* **4** 2957–63
- [51] Wang Y, Shang S L, Chen L Q and Liu Z K 2011 Magnetic excitation and thermodynamics of BaFe2As2 *Int. J. Quantum Chem.* **111** 3565–70
- [52] Yu Y and Kivelson S A 2019 Fragile superconductivity in the presence of weakly disordered charge density waves *Phys. Rev. B* **99** 144513
- [53] Norman M R 2021 Fragile superconductivity at high magnetic fields *Proc. Natl. Acad. Sci.* **118** e2100372118
- [54] Lu Z W and Klein B M 1997 Anharmonic effects in the A15 compounds induced by sublattice distortions *Phys. Rev. Lett.* **79** 1361–4
- [55] Li Y and Gao Y 2017 GLAG theory for superconducting property variations with A15 composition in Nb3Sn wires *Sci. Rep.* **7** 1133
- [56] Liu Z-K 2023 Thermodynamics and its prediction and CALPHAD modeling: Review, state of the art, and perspectives *Calphad* **82** 102580

Supplementary Material

Symmetry-broken superconducting configurations from density functional theory for bcc and hcp metals and Nb₃Sn

Shun-Li Shang and Zi-Kui Liu

Department of Materials Science and Engineering, The Pennsylvania State University,
University Park, PA 16802, USA

1 Supplementary Tables

Table S 1. Settings used to generate SCCs, perform DFT-based calculations, and plot electron SNCDDs, including the crystal structures (str.), the initial atomic perturbation δ_{ini} (cf., Eq. 4), X-C functionals, k -point meshes, cutoff energy (E_{cut} in eV, determined by the VASP setting “PREC = High”), the minimum (F_{min}) and maximum (F_{max}) charge density differences, and the contour levels for plotting electron SNCDDs (F_{level}) with charge gain.

Materials	Str.	δ_{ini}	X-C	k -mesh	E_{cut}	F_{min}	F_{max}	F_{level}	Figure
Be_sv (4) ^a	hcp	0.04	r ² SCAN	7×7×7	401.4	-0.300982	0.316675	0.000314	Figure S 1
Mg_pv (8) ^a	hcp	0.06	PBE	7×7×7	525.1	-0.213652	0.214463	0.0001408	Figure 1
			r ² SCAN			-0.320174	0.313314	0.00021	Figure S 2
Sc_sv (11) ^a	hcp	0.02	r ² SCAN	7×7×7	289.5	-0.112994	0.111195	0.00018	Figure S 3
Y_sv (11) ^a	hcp	0.04	r ² SCAN	7×7×7	263.4	-0.0605017	0.0599861	0.000188	Figure S 4
Ti_pv (10) ^a	hcp	0.08	r ² SCAN	7×7×7	289.0	-0.204697	0.204974	0.00061	Figure S 5
Zr_sv (12) ^a	hcp	0.04	r ² SCAN	7×7×7	298.9	-0.0701622	0.069794	0.00048	Figure S 6
Hf_pv (10) ^a	hcp	0.04	r ² SCAN	7×7×7	286.4	-0.0450728	0.0442788	0.00058	Figure S 7
Tc_pv (13) ^a	hcp	0.02	r ² SCAN	7×7×7	342.6	-0.0663961	0.0665165	0.0011	Figure S 8
Re_pv (13) ^a	hcp	0.04	r ² SCAN	7×7×7	294.1	-0.110753	0.109115	0.00325	Figure S 9
Ru_pv (14) ^a	hcp	0.06	r ² SCAN	7×7×7	312.1	-0.0729848	0.0731499	0.00138	Figure S 10
Os_pv (14) ^a	hcp	0.04	r ² SCAN	7×7×7	296.4	-0.0748346	0.0747532	0.00182	Figure S 11
Zn (12) ^a	hcp	0.06	r ² SCAN	7×7×7	359.7	-0.248358	0.241290	0.00078	Figure S 12
V_pv (11) ^a	bcc	0.04	PBE	7×7×7	342.8	-0.143164	0.138092	0.00031	Figure S 13
			r ² SCAN			-0.179615	0.186421	0.014	Figure 2
Nb_pv (11) ^a	bcc	0.02	r ² SCAN	7×7×7	271.2	-0.0171389	0.0169606	0.00019	Figure S 14
Ta_pv (11) ^a	bcc	0.04	r ² SCAN	7×7×7	290.8	-0.0445001	0.0445570	0.000425	Figure S 15
Mo_pv (12) ^a	bcc	0.02	r ² SCAN	7×7×7	292.0	-0.0217756	0.0218054	0.00042	Figure S 16
W_sv (14) ^a	bcc	0.04	r ² SCAN	7×7×7	290.0	-0.0837359	0.0838688	0.00095	Figure S 17
Nb ₃ Sn ^b	A15		PBE	7×7×7	313.4	-0.0233904	0.0181413	0.0021	Figure 4

^a Valence electrons used in the present DFT calculations. In addition, the suffixes “_sv, _pv, or _d” after the symbols of some elements indicate the s, p, and d states are considered as valence states.

^b For element Sn_d, 14 valence electrons were included.

Table S 2. Atomic displacements between the NCC and SCC, including the crystal structures (str.), the X-C functionals, the average atomic displacement vector (Δx , Δy , Δz), and the corresponding magnitude of atomic movement ΔR (see Eq. 5). Values following the \pm symbol denote the standard deviation σ .

Materials	Str.	X-C	$\Delta R \pm \sigma$ (Å)	$\Delta x \pm \sigma$ (Å)	$\Delta y \pm \sigma$ (Å)	$\Delta z \pm \sigma$ (Å)
Be	hcp	r ² SCAN	0.0481 \pm 6.6E-5 0.0256 \pm 2.0E-4	0.0398 \pm 5.8E-5 0.0205 \pm 1.2E-4	-0.0204 \pm 1.1E-5 -0.0057 \pm 1.5E-4	0.0176 \pm 3.0E-5 0.0142 \pm 0.2E-4
Mg	hcp	PBE	0.0420 \pm 6.5E-5 0.0427 \pm 6.1E-4	0.0400 \pm 3.9E-5 0.0400 \pm 1.2E-5	-0.0128 \pm 0.6E-5 -0.0149 \pm 0.3E-5	0.0004 \pm 5.2E-5 -0.0004 \pm 5.1E-5
		r ² SCAN	0.0426 \pm 0.0178 0.0493 \pm 0.0184	0.0399 \pm 0.0057 0.0478 \pm 0.0095	-0.0149 \pm 0.0047 -0.0108 \pm 0.0018	-0.0004 \pm 0.0161 -0.0055 \pm 0.0156
Sc	hcp	r ² SCAN	0.0444 \pm 17E-4	0.0028 \pm 0.0013	-0.0336 \pm 0.0006	-0.0288 \pm 0.0010
Y	hcp	r ² SCAN	0.0591 \pm 6.0E-4	0.0490 \pm 4.0E-4	-0.0212 \pm 1.2E-4	0.0252 \pm 4.4E-4
Ti	hcp	r ² SCAN	0.0978 \pm 7.8E-4	0.0489 \pm 4.4E-4	-0.0847 \pm 0.3E-5	0.0000 \pm 6.5E-4
Zr	hcp	r ² SCAN	0.0524 \pm 1.9E-4	0.0432 \pm 1.4E-4	-0.0187 \pm 0.9E-4	0.0229 \pm 0.9E-4
Hf	hcp	r ² SCAN	0.0514 \pm 4.0E-4	0.0425 \pm 3.0E-4	-0.0184 \pm 1.9E-4	-0.0223 \pm 1.9E-4
Tc	hcp	r ² SCAN	0.0369 \pm 0.0012	0.0023 \pm 0.0003	-0.0276 \pm 0.0000	-0.0243 \pm 0.0011
Re	hcp	PBE	0.0450 \pm 9.6E-4	0.0370 \pm 2.6E-4	-0.0160 \pm 1.0E-4	0.0199 \pm 9.2E-4
	hcp	r ² SCAN	0.0447 \pm 0.0498 0.0447 \pm 0.0108	0.0368 \pm 0.0001 0.0368 \pm 0.0108	-0.0160 \pm 0.0000 -0.0158 \pm 0.0000	0.0198 \pm 0.0498 0.0199 \pm 0.0005
Ru	hcp	r ² SCAN	0.0358 \pm 6.5E-5	0.0338 \pm 5.4E-5	-0.0117 \pm 0.1E-5	0.0000 \pm 3.7E-5
Os	hcp	r ² SCAN	0.0442 \pm 6.0E-5	0.0366 \pm 4.2E-5	-0.0158 \pm 1.0E-5	0.0192 \pm 4.1E-5
Zn	hcp	r ² SCAN	0.0449 \pm 1.0E-4 0.0330 \pm 6.6E-4	0.0331 \pm 8.5E-5 0.0321 \pm 0.7E-4	-0.0303 \pm 0.4E-5 0.0077 \pm 0.1E-4	0.0000 \pm 5.3E-5 0.0000 \pm 6.5E-4
V	bcc	PBE	0.0426 \pm 11E-4	0.0400 \pm 7.5E-4	-0.0133 \pm 8.5E-4	-0.0067 \pm 0.7E-4
		r ² SCAN	0.0425 \pm 3.6E-4	0.0398 \pm 2.7E-4	-0.0133 \pm 1.8E-4	-0.0067 \pm 1.7E-4
Nb	bcc	r ² SCAN	0.0180 \pm 1.8E-4	-0.0147 \pm 1.0E-4	0.0074 \pm 1.0E-4	-0.0074 \pm 1.1E-4
Ta	bcc	r ² SCAN	0.0470 \pm 2.1E-4	0.0441 \pm 0.4E-4	-0.0147 \pm 1.5E-4	-0.0073 \pm 1.4E-4
Mo	bcc	r ² SCAN	0.0172 \pm 6.4E-5	-0.0140 \pm 2.1E-5	0.0070 \pm 4.0E-5	-0.0070 \pm 4.5E-5
W	bcc	r ² SCAN	0.0451 \pm 2.6E-4	0.0423 \pm 1.5E-4	-0.0141 \pm 1.5E-4	-0.0070 \pm 1.5E-4
Nb ₃ Sn ^a	A15	PBE	0.0233	0.0233	0	0

^a Displacement is only for Wyckoff site 4j (x, 0, 0).

2 Supplementary Figures

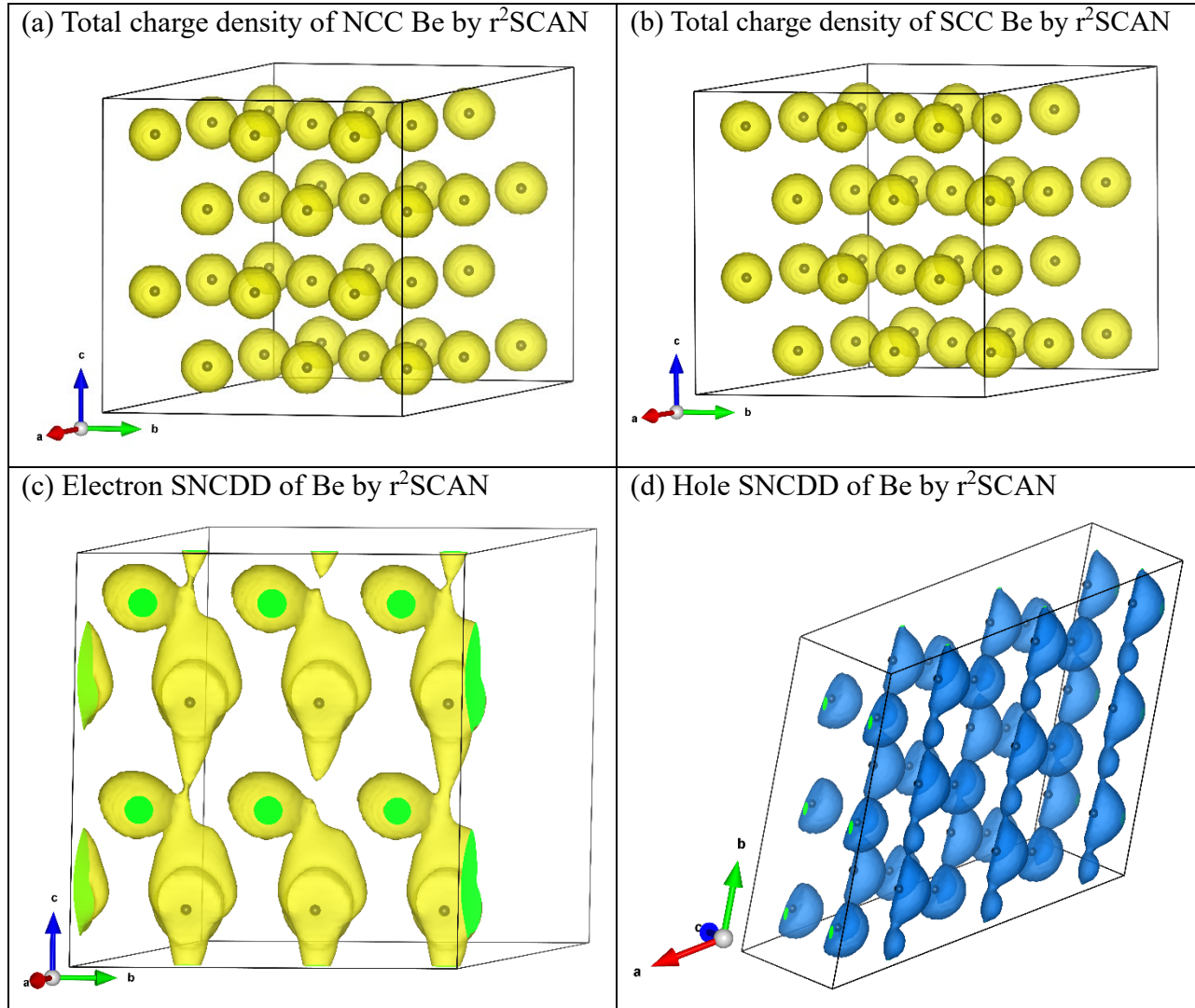
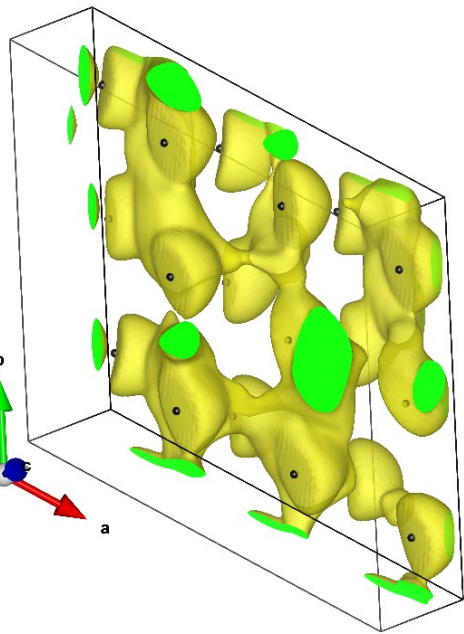


Figure S 1. (a) Total charge density of Be with NCC configuration and (b) total charge density of Be with SCC configuration. Partial electron (c, yellow) and hole (d, blue) SNCDDs of Be predicted by r^2 SCAN, showing the SODTs along the *c*-axis for electron (c) and the *b*-axis for hole (d). In contrast, GGA-PBE predicts that both electron and hole SNCDDs show SODTs along the *b*-axis direction (figures not shown).

(a) Electron SNCDD of Mg by r^2 SCAN



(d) Hole SNCDD of Mg by r^2 SCAN

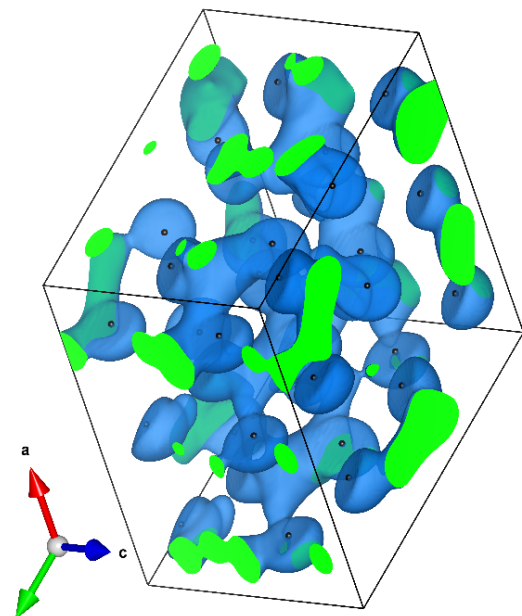
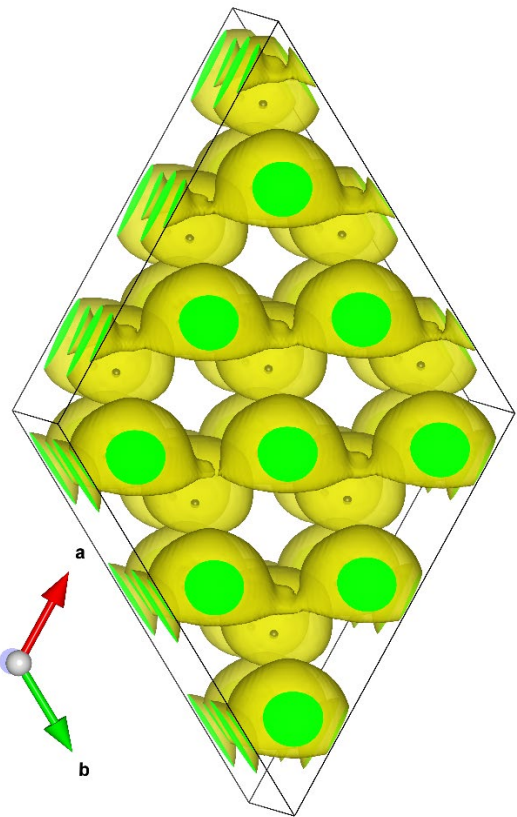


Figure S 2. Partial electron (a, yellow) and hole (b, blue) SNCDDs of Mg predicted by GGA- r^2 SCAN, showing a pronounced zigzag pattern for the electron SNCDD for electron and a 3D characteristics for the hole SNCDD; see the predictions by GGA-PBE in Figure 1.

(a) Electron SNCDD of Sc by r^2 SCAN



(b) Hole SNCDD of Sc by r^2 SCAN

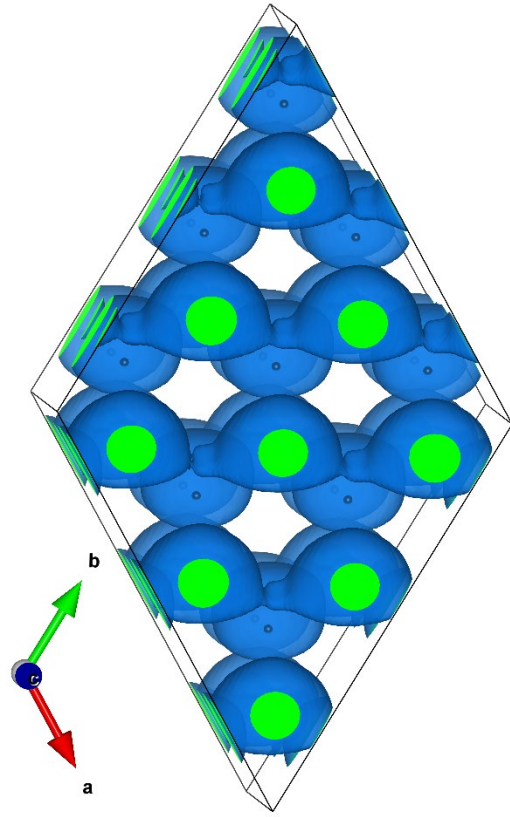
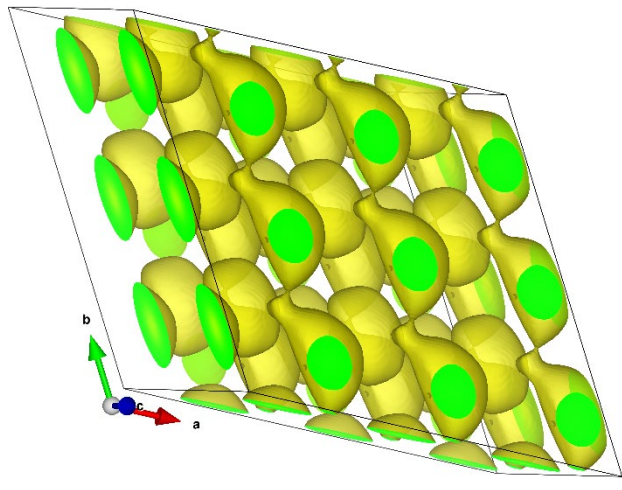


Figure S 3. Electron (a, yellow) and hole (b, blue) SNCDDs of Sc predicted by r^2 SCAN, showing SODTs along [110]. Note that GGA-PBE predicts similar characteristics (not shown).

(a) Electron SNCDD of Y by r^2 SCAN



(b) Hole SNCDD of Y by r^2 SCAN

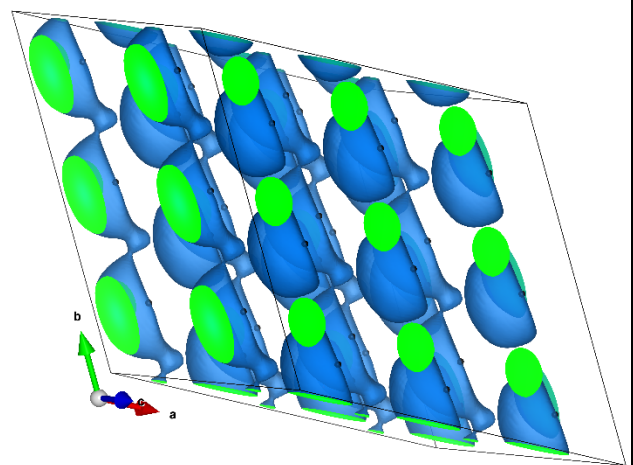
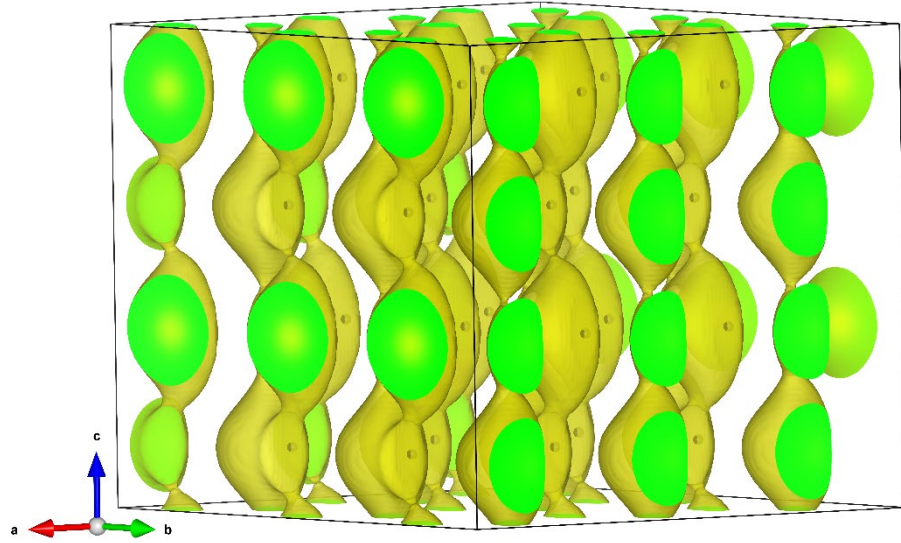


Figure S 4. Electron (a, yellow) and hole (b, blue) SNCDDs of Y predicted by r^2 SCAN, showing SODTs along the b-axis. Note that GGA-PBE predicts similar characteristics (not shown).

(a) Electron SNCDD of Ti by r^2 SCAN



(b) Hole SNCDD of Ti by r^2 SCAN

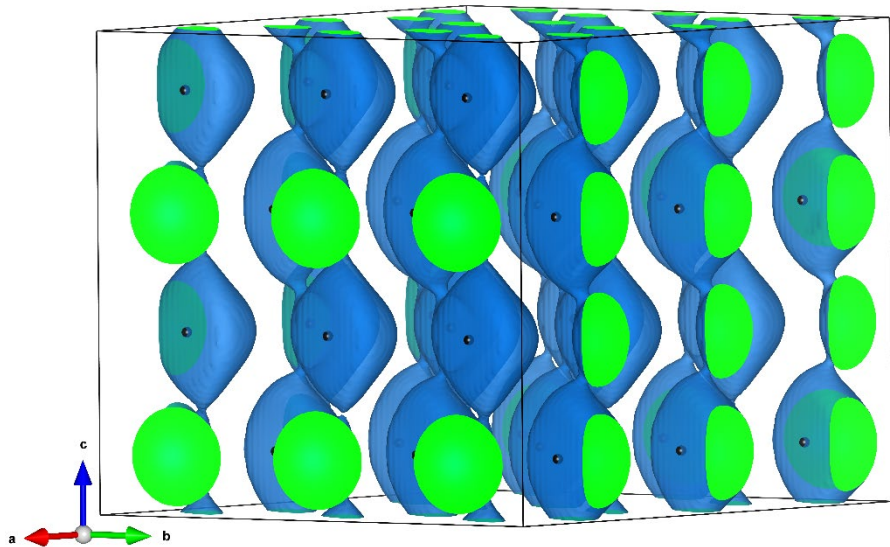
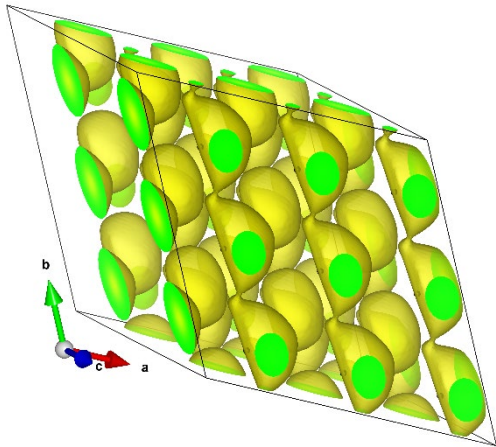


Figure S 5. Electron (a, yellow) and hole (b, blue) SNCDDs of Ti predicted by r^2 SCAN, showing SODTs along the c-axis. Note that GGA-PBE predicts similar characteristics (not shown).

(a) Electron SNCDD of Zr by r^2 SCAN



(b) Hole SNCDD of Zr by r^2 SCAN

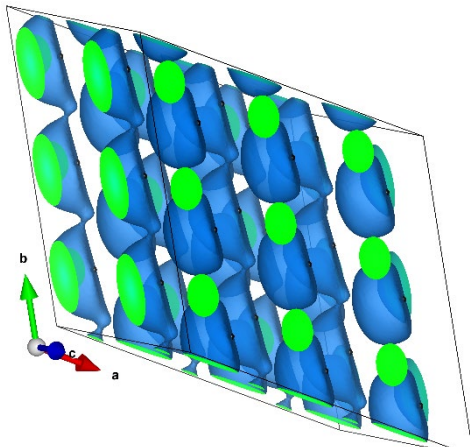
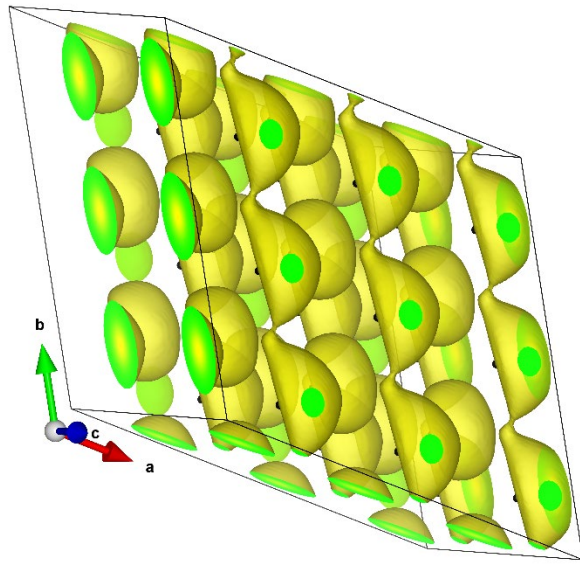


Figure S 6. Electron (a, yellow) and hole (b, blue) SNCDDs of Zr predicted by r^2 SCAN, showing SODTs along the b -axis. Note that GGA-PBE predicts similar characteristics (not shown).

(a) Electron SNCDD of Hf by r^2 SCAN



(b) Hole SNCDD of Hf by r^2 SCAN

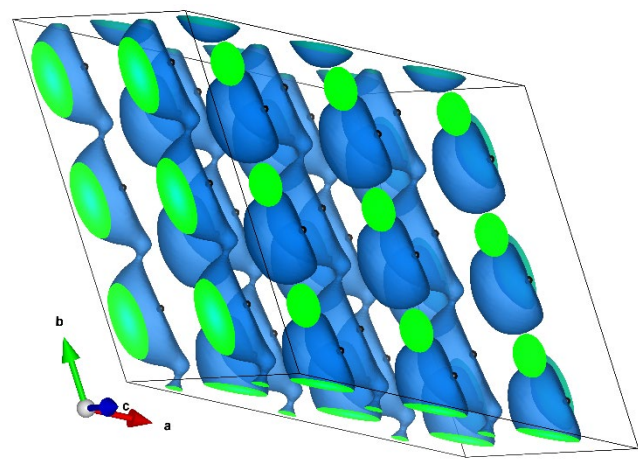


Figure S 7. Electron (a, yellow) and hole (b, blue) SNCDDs of Hf predicted by r^2 SCAN, showing SODTs along the b -axis. Note that GGA-PBE predicts similar characteristics (not shown).

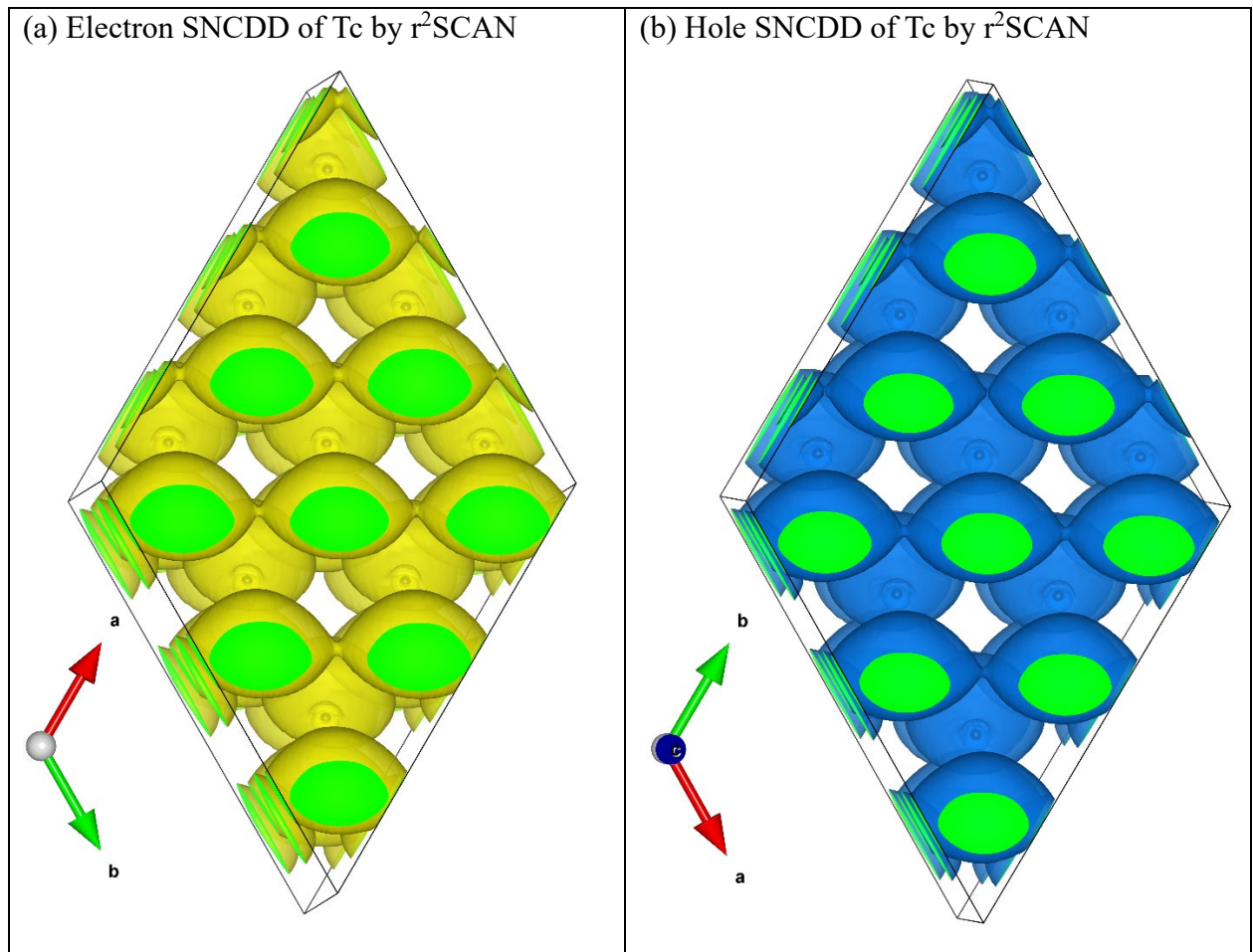


Figure S 8. Electron (a, yellow) and hole (b, blue) SNCDDs of Tc predicted by r^2 SCAN, viewed along the c -axis, showing SODTs along $[110]$. Note that GGA-PBE predicts similar characteristics (not shown).

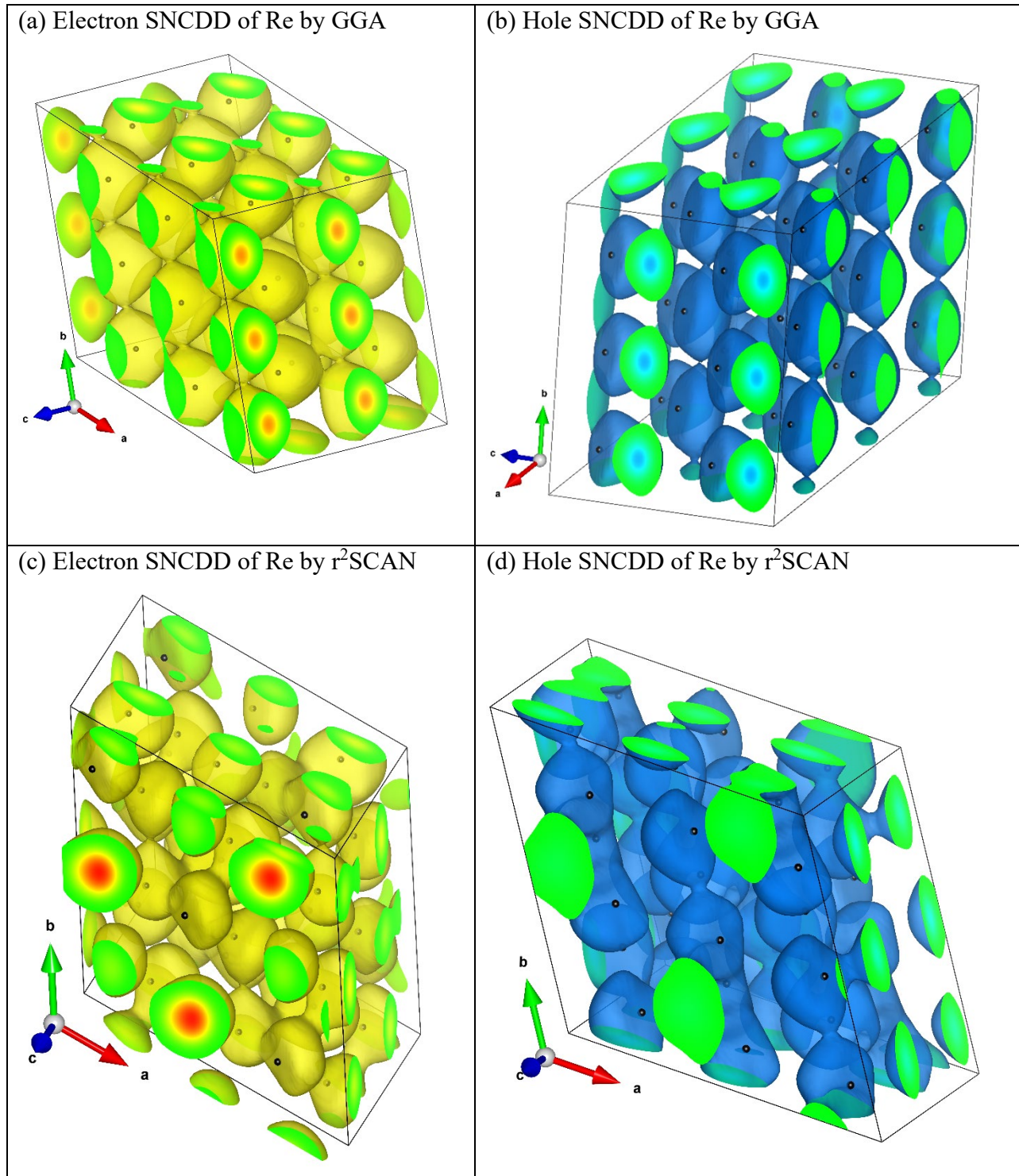


Figure S 9. Electron (a, yellow) and hole (b, blue) SNCDDs of Re predicted by GGA-PBE, showing SODTs along the b-axis direction. However, r^2 SCAN does not predict SODTs for Re, see (c) and (d).

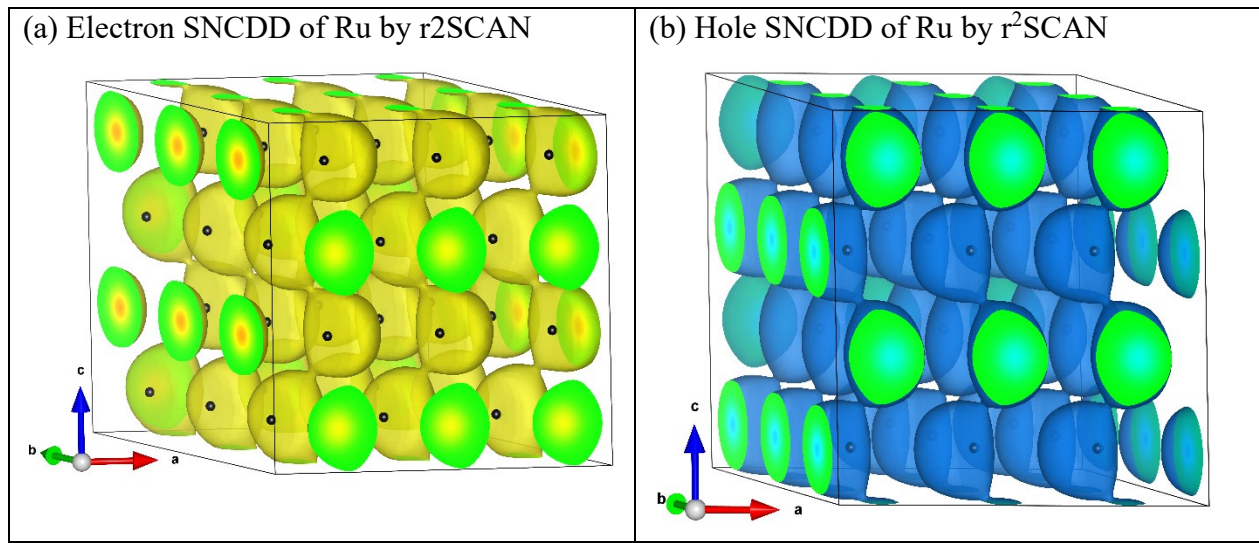


Figure S 10. Electron (a, yellow) and hole (b, blue) SNCDDs of Ru predicted by $r^2\text{SCAN}$, showing SODTs along the c -axis direction with zigzag characters. Note that GGA-PBE predicts similar characteristics (not shown).

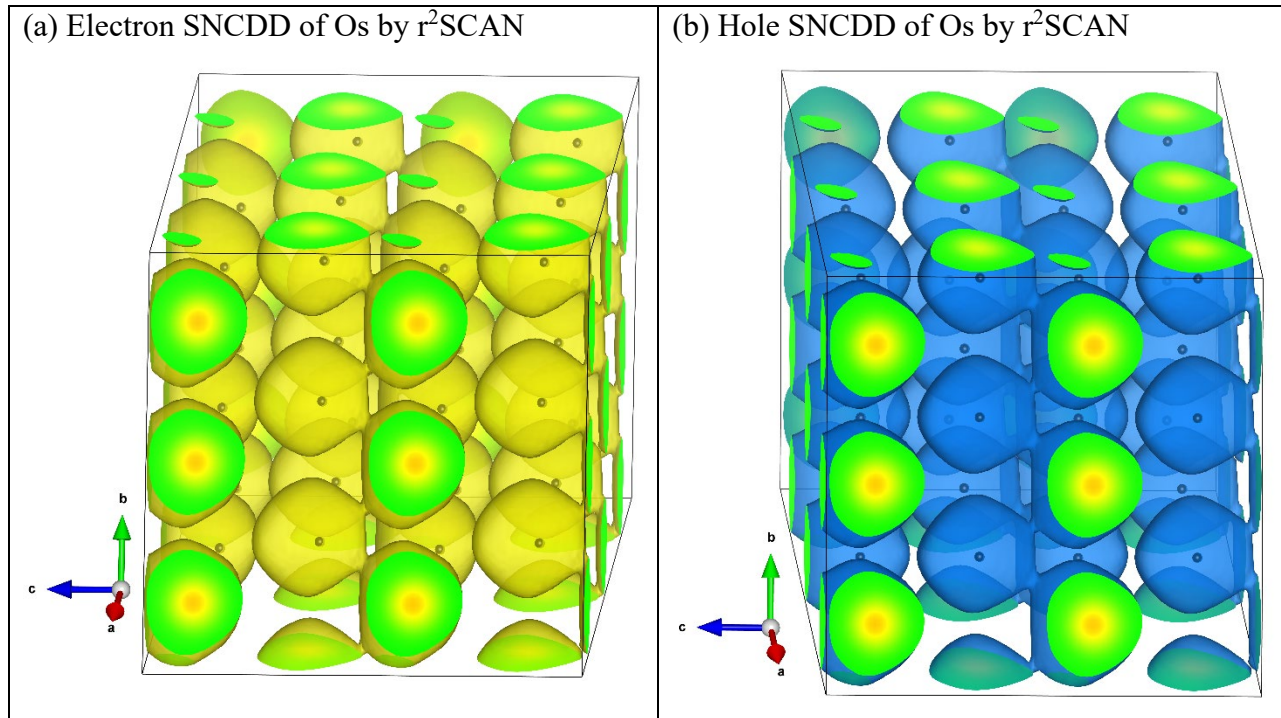


Figure S 11. Electron (a, yellow) and hole (b, blue) SNCDDs of Os predicted by $r^2\text{SCAN}$, showing SODTs along the b-axis. Note that GGA-PBE predicts similar characteristics (not shown).

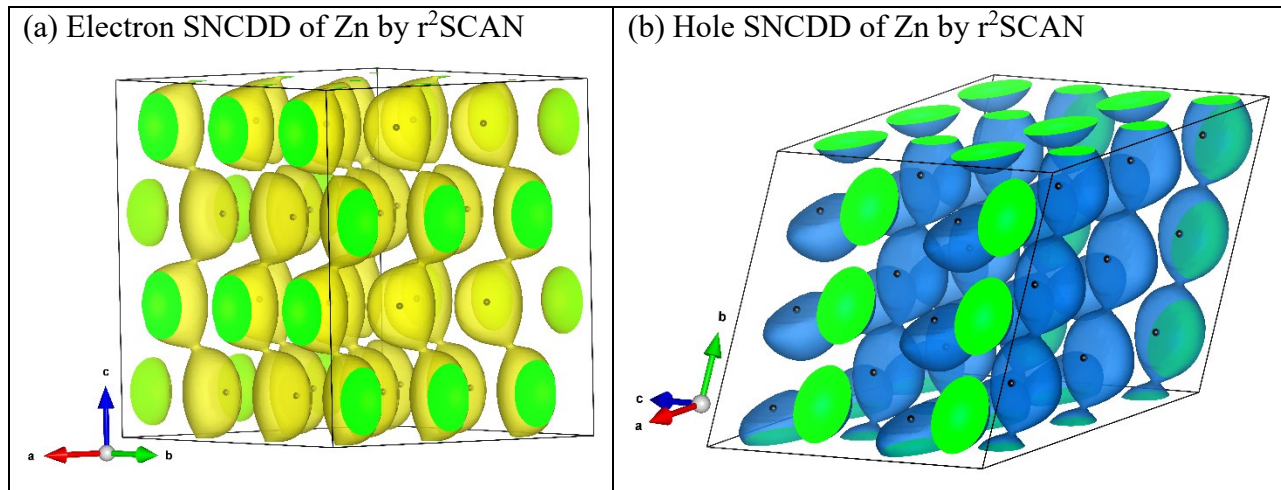


Figure S 12. Electron (a, yellow) and hole (b, blue) SNCDDs of Zn predicted by $r^2\text{SCAN}$, showing SODTs along the b-axis (or the c-axis for electron). Note that GGA-PBE predicts similar characteristics with the formed SODTs along the b-axis (not shown).

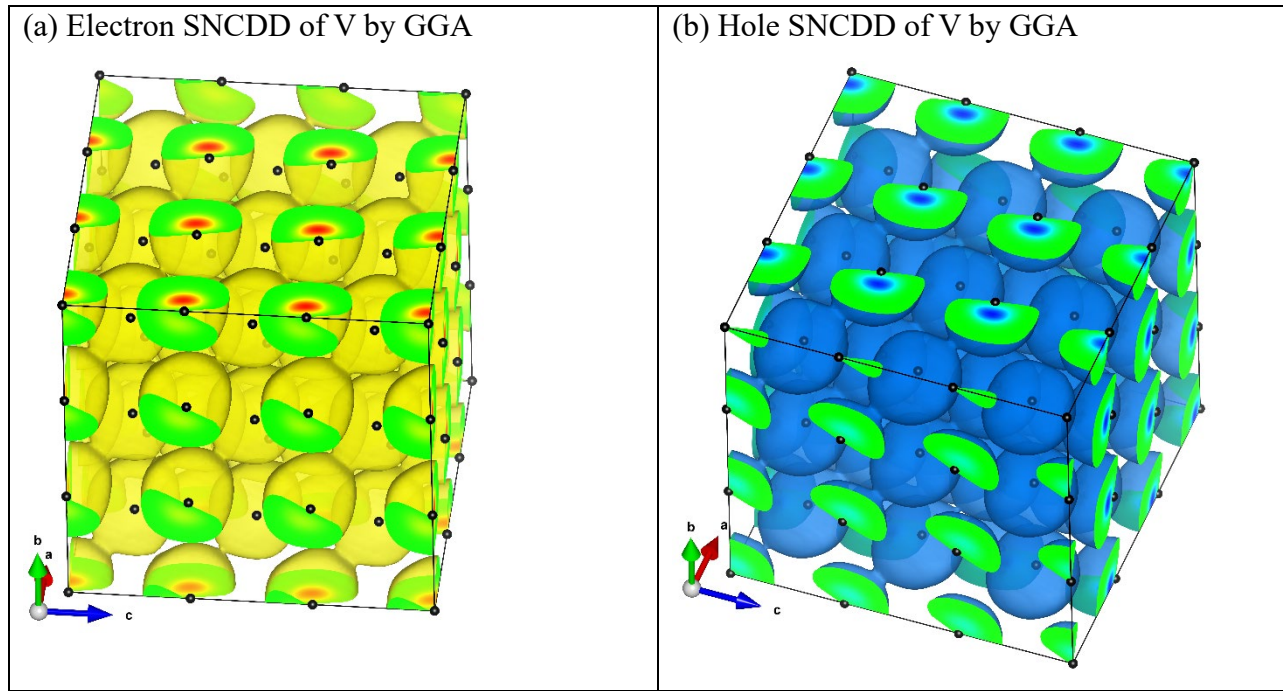


Figure S 13. Electron (a, yellow) and hole (b, blue) SNCDDs of V predicted by GGA-PBE, showing SODTs along [111]. Note that r^2 SCAN predictions are shown in Figure 2.

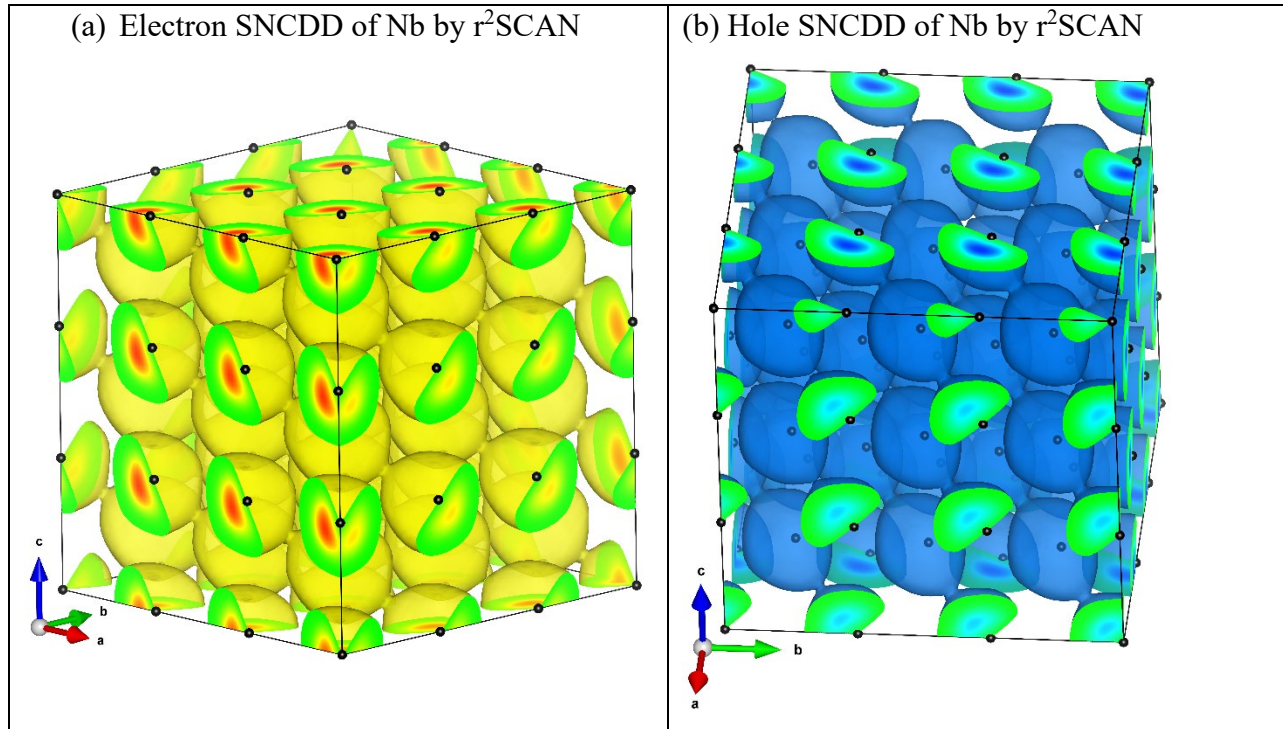
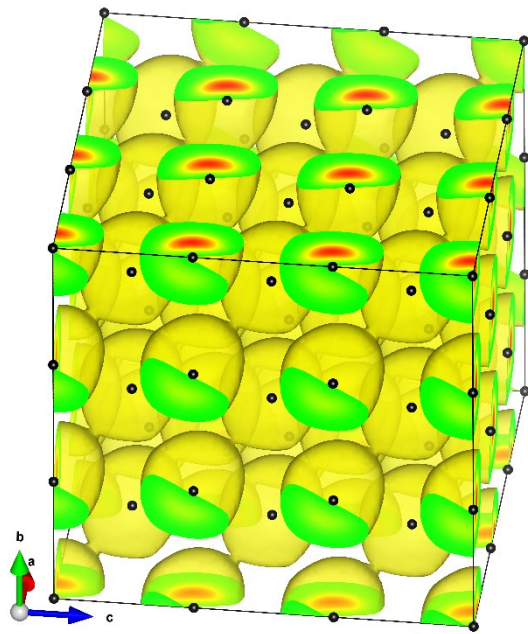


Figure S 14. Electron (a, yellow) and hole (b, blue) SNCDDs of Nb predicted by r^2 SCAN, showing SODTs along [111]. Note that GGA-PBE predicts similar characteristics (not shown).

(a) Electron SNCDD of Ta by r^2 SCAN



(b) Hole SNCDD of Ta by r^2 SCAN

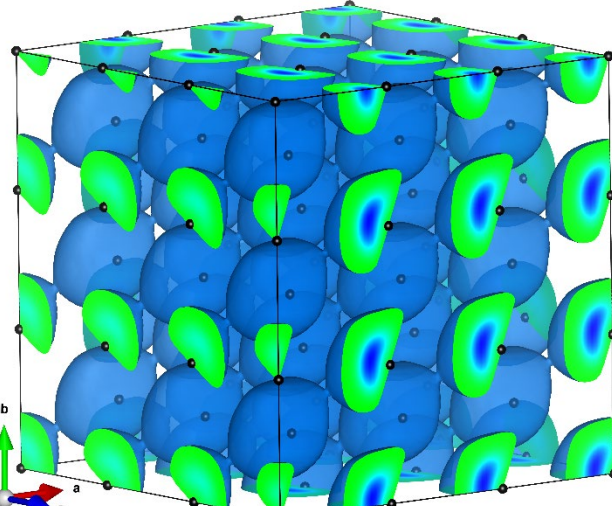


Figure S 15. Electron (a, yellow) and hole (b, blue) SNCDDs of Ta predicted by r^2 SCAN, showing SODTs along [111]. Note that GGA-PBE predicts similar characteristics (not shown).

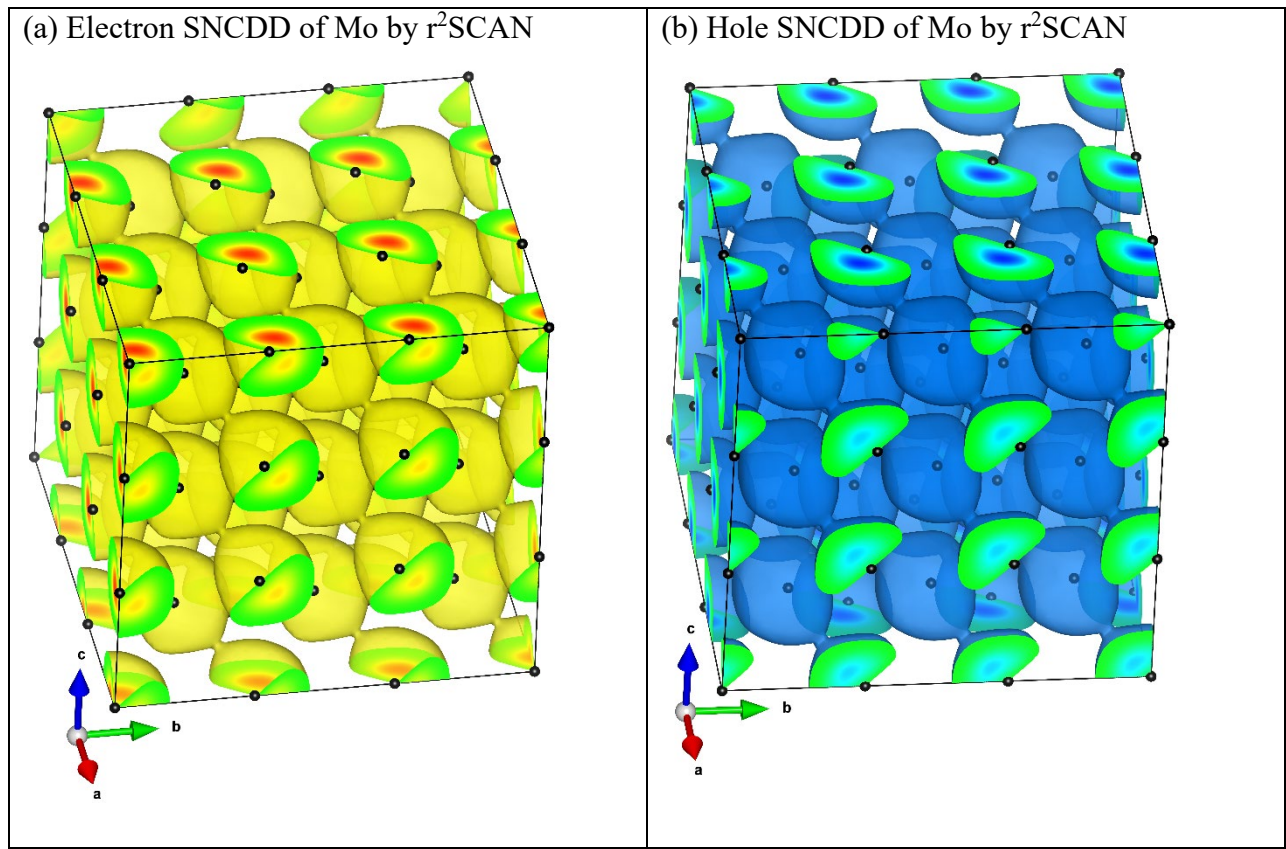


Figure S 16. Electron (a, yellow) and hole (b, blue) SNCDDs of Mo predicted by r^2 SCAN, showing SODTs along $[1\bar{1}1]$. Note that GGA-PBE predicts roughly similar characteristics but not as clear as the r^2 SCAN cases.

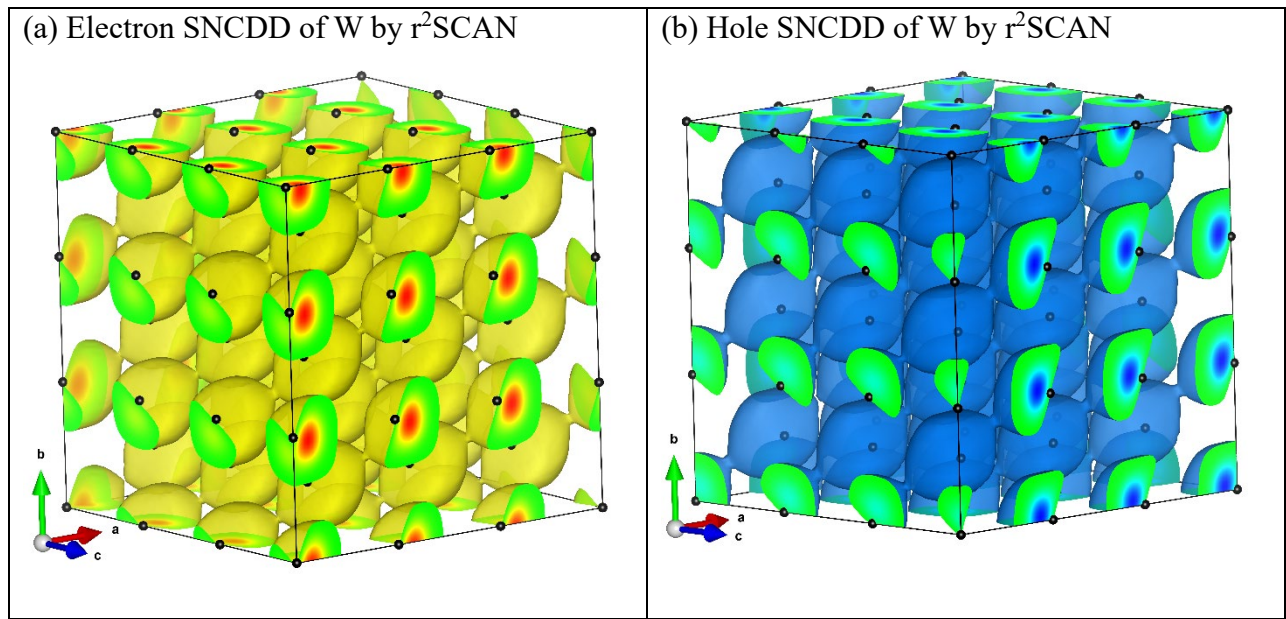


Figure S 17. Electron (a, yellow) and hole (b, blue) SNCDDs of W predicted by r^2SCAN , showing SODTs along [111]. Note that GGA-PBE predicts similar characteristics.